

DC-Net: Divide-and-Conquer for Salient Object Detection

Jiayi Zhu
MBZUAI
Abu Dhabi, UAE
zjyztzhujiayi55@gmail.com

Xuebin Qin
MBZUAI
Abu Dhabi, UAE
xuebinua@gmail.com

Abdulmotaieb Elsaddik
MBZUAI
Abu Dhabi, UAE
a.elsaddik@mbzuai.ac.ae

Abstract

In this paper, we introduce Divide-and-Conquer into the salient object detection (SOD) task to enable the model to learn prior knowledge that is for predicting the saliency map. We design a novel network, Divide-and-Conquer Network (DC-Net) which uses two encoders to solve different subtasks that are conducive to predicting the final saliency map, here is to predict the edge maps with width 4 and location maps of salient objects and then aggregate the feature maps with different semantic information into the decoder to predict the final saliency map. The decoder of DC-Net consists of our newly designed two-level Residual nested-ASPP (ResASPP²) modules, which have the ability to capture a large number of different scale features with a small number of convolution operations and have the advantages of maintaining high resolution all the time and being able to obtain a large and compact effective receptive field (ERF). Based on the advantage of Divide-and-Conquer's parallel computing, we use Parallel Acceleration to speed up DC-Net, allowing it to achieve competitive performance on six LR-SOD and five HR-SOD datasets under high efficiency (60 FPS and 55 FPS). Codes and results are available: <https://github.com/PiggyJerry/DC-Net>.

1. Introduction

Recently, with the development of deep convolutional neural networks (CNNs), downstream computer vision tasks have been greatly improved, and Salient Object Detection (SOD) has also benefited from it. The purpose of SOD is to segment the most visually attractive part of an image, and it is widely used in 3D modeling, image editing, art design materials, AR and 3D rendering. So what are the deficiencies worthy of researchers to explore? Next, we will discuss it based on the previous method.

In recent years, several deep salient object detection methods have introduced different auxiliary maps (e.g. edge maps, body maps, and detail maps) to assist in generating saliency maps, and their designs fall into the following three

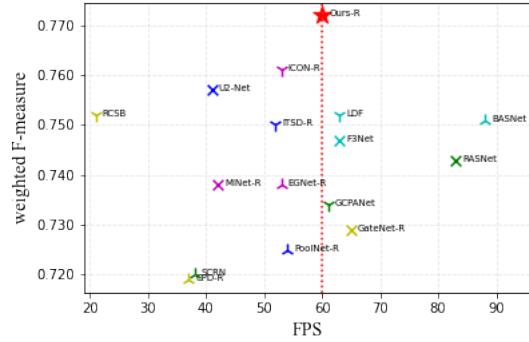


Figure 1. Comparison of FPS and performance of our DC-Net-R with other state-of-the-art SOD convolution-based methods. The F_{β}^w measure is computed on dataset DUT-OMRON [61]. The red star denotes our DC-Net-R (Ours-R, 60 FPS) and the red dot line denotes the real-time (60 FPS) line.

categories. First, after feeding the image into an encoder, use the features learned by predicting different auxiliary maps to assist in predicting the saliency maps [26, 67]. The second is to use auxiliary maps as input to guide the training process [48]. The third is to make the models pay more attention to the edge pixels through the boundary-aware loss [41, 14]. However, these methods have some limitations. For the first method, a single encoder with multiple heads to learn different semantic information may not fully represent all the different semantic information [54, 56]. Moreover, when multiple branches need to interact with each other with a sequence, they cannot be accelerated through parallelism, leading to low efficiency [69]. The second method suffers from the need to generate auxiliary maps during the inference stage, leading to low efficiency. The third method can only use the boundary information. It is more intuitive and effective to directly use auxiliary maps for training.

This leads to our first question: **can we design an end-to-end network to use multiple encoders to represent the different semantic information of the saliency map to learn the prior knowledge before predicting the saliency map and be efficient?**

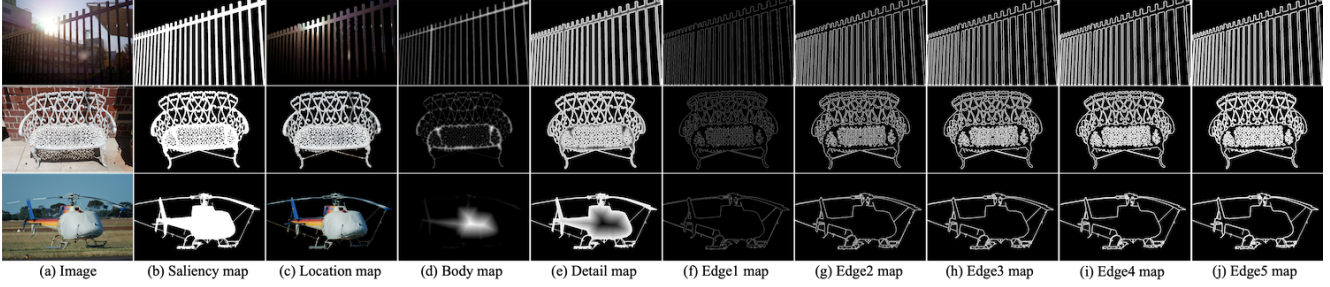


Figure 2. Some examples of different auxiliary maps. (c) represents the location information of the salient object. The sum of (d) and (e) is equal to (b). (f)-(j) represents the edge pixels of salient objects with widths 1, 2, 3, 4, and 5 respectively.

Current mainstream pixel-level deep CNNs such as U-Net [42] and feature pyramid network (FPN) [25] increase the receptive field and improve efficiency through continuous pooling layers or convolutional layers with stride of 2, while pooling operation can lose detail information, that is, sacrifice the high resolution of the feature maps, and convolution with stride of 2 results in no convolution operation on half the pixels. Dilated convolution and atrous spatial pyramid pooling (ASPP) are proposed by Deeplab [3] for this problem, but due to the large gap in the atrous rate and only one parallel convolutional layer, the pixel sampling is sparse. A recently proposed method U²-Net [40] proposes a Residual U-blocks (RSU), and it can obtain multi-scale feature maps after several pooling layers at each stage, and finally restore to the high resolution of the current stage like U-Net, but the pooling operation still leads to the loss of detail information in this process.

Therefore, our second question is: **can we design a module to obtain a larger receptive field with fewer convolutional layers while maintaining the high resolution of the feature maps of the current stage all the time?**

Our main contribution is a novel method for SOD, called Divide-and-Conquer Network (**DC-Net**) with a two-level Residual nested-ASPP module (**ResASPP²**), which solves the two issues raised above, and we introduce **Parallel Acceleration** into DC-Net to speed it up. Our network training process is as follows: after feeding the image into two identical encoders, edge maps with width 4 and the location maps are used to supervise the two encoders respectively, as shown in Fig. 2 (i) and (c), and then the concatenation of the feature maps of the two encoders are fed into the decoder composed of ResASPP²s to predict the final saliency maps in the way of U-Net like structure. ResASPP² obtains a large and compact effective receptive field (ERF) without sacrificing high resolution by nesting two layers of parallel convolutional layers with dilation rates {1, 3, 5, 7}. Additionally, its output feature map has much diversity by fusing a large number of feature maps with different scales and compact pixel sampling. Parallel Acceleration merges two identical encoders into an encoder with the same structure, which is called **Parallel Encoder**. ResASPP² is simplified

by our implementation of **Merged Convolution**. Our DC-Net achieves competitive performance against the state-of-the-art (SOTA) methods on five public SOD datasets and runs at real-time (60 FPS based on **Parallel-ResNet-34**, with input size of $352 \times 352 \times 3$; 55 FPS based on **Parallel-ResNet-34**, with input size of $1024 \times 1024 \times 3$; 29 FPS based on **Parallel-Swin-B**, with input size of $384 \times 384 \times 3$) on a single RTX 6000 GPU.

2. Related Works

Under the increasing demand for higher efficiency and accuracy in the real world, traditional methods [17, 61, 30] based on hand-crafted features are gradually losing competitiveness. In recent years, more and more deep salient object detection networks [16, 65] have been proposed, and a lot of research has been done on how to integrate multi-level and multi-scale features [23], and how to use the auxiliary maps such as the edge map to train the network [67].

Multi-level and multi-scale feature integration: Recent works such as U-Net [42], Feature Pyramid Network (FPN) [25], PSPNet [66] and Deeplab [3] have shown that the fusion of multi-scale contextual features can lead to better results. Many subsequent developed methods for SOD to integrate or aggregate multi-level and multi-scale features were inspired by them to some extent. Liu *et al.* (PoolNet) [26] aggregate the multi-scale features obtained from a module adapted from pyramid pooling module at each level of the decoder and a global guidance module is introduced to help each level obtain better location information. Wei *et al.* (F³Net) [53] propose a feature fusion strategy that is different from addition or concatenation, which can adaptively select fused features and reduce redundant information. Mohammadi *et al.* (CAGNet) [34] propose a multi-scale feature extraction module that combines convolutions with different sizes of convolution kernels in parallel. Zhao *et al.* (GateNet) [68] propose a Fold-ASPP module to generate finer multi-scale advanced saliency features. Zhuge *et al.* (ICON) [70] make full use of the features under various receptive fields to improve the diversity of features, and introduce an attention module to enhance feature chan-

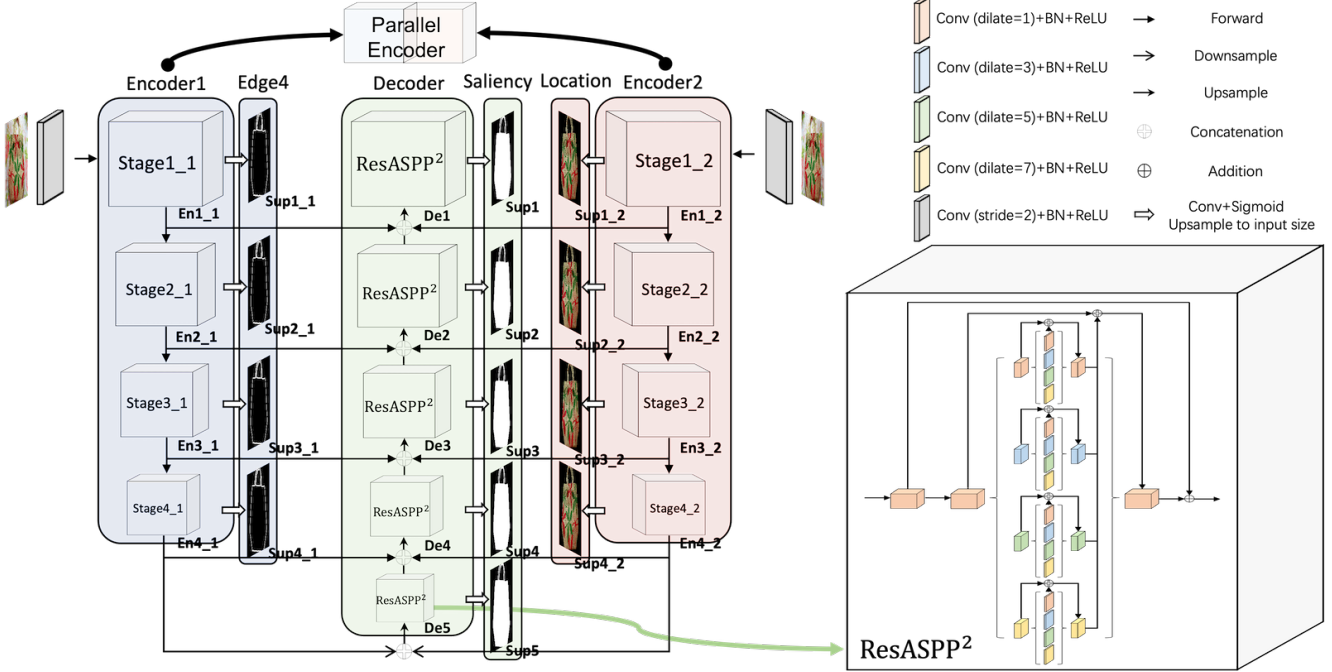


Figure 3. Illustration of our proposed DC-Net architecture. DC-Net has two encoders and a decoder, we can consider these two encoders as one parallel encoder. Thus, the main architecture of DC-Net is a U-Net like Encoder-Decoder, where each stage of the decoder consists of our newly proposed two-level Residual nested-ASPP module (ResASPP^2).

nels that the integral salient objects are highlighted. Chen *et al.* (GCPANet) [6] integrate global context features with low- and high-level features. Wu *et al.* (CPD) [55] propose a framework for fast and accurate salient object detection named Cascaded Partial Decoder. Pang *et al.* (MINet) [36] propose the aggregate interaction modules and self-interaction modules to integrate the features from adjacent levels and obtain more efficient multi-scale features from the integrated features. Chen *et al.* (RASNet) [5] employ residual learning to refine saliency maps progressively and design a novel top-down reverse attention block to guide the residual learning. Qin *et al.* (U^2 -Net) [40] propose Residual U-blocks (RSU) to capture more contextual information from different scales and increase the depth of the whole architecture without significantly increasing the computational cost. Xie *et al.* (PGNet) [57] integrates the features extracted by the Transformer and CNN backbones, enabling the network to combine the detection ability of Transformer with the detailed representation ability of CNN.

Utilizing auxiliary supervision: Many auxiliary maps such as edge maps, body maps and detail maps have been introduced to assist in predicting the saliency map for SOD in recent years. Liu *et al.* (PoolNet) [26] fuses edge information with saliency predictions in a multi-task training manner. Zhao *et al.* (EGNet) [67] perform interactive fusion after explicit modeling of salient objects and edges to jointly optimize the tasks of salient object detection and

edge detection under the belief that these two tasks are complementary. Qin *et al.* (BASNet) [41] propose a hybrid loss which can focus on the pixel-level, patch-level, and map-level salient parts of the image. Su *et al.* (BANet) [47] use the selective features of boundaries to slight appearance change to distinguish salient objects and background. Feng *et al.* (AFNet) [14] design the Attentive Feedback Modules (AFMs) and a Boundary-Enhanced Loss (BEL) to better explore the structure of objects and learn exquisite boundaries respectively. Wu *et al.* (SCRN) [56] propose a stacking Cross Refinement Unit (CRU) to simultaneously refine multi-level features of salient object detection and edge detection. Wei *et al.* (LDF) [54] explicitly decompose the original saliency map into body map and detail map so that edge pixels and region pixels have a more balanced distribution. Ke *et al.* (RCSB) [18] propose a contour-saliency blending module to exchange information between contour and saliency. Zhou *et al.* (ITSD) [69] propose an interactive two-stream decoder to explore multiple cues, including saliency, contour and their correlation. Qin *et al.* (IS-Net) [39] propose a simple intermediate supervision baseline using both feature-level and mask-level guidance for model training.

3. Proposed Method

First, we introduce our proposed Divide-and-Conquer Network and then describe the details of the two-level

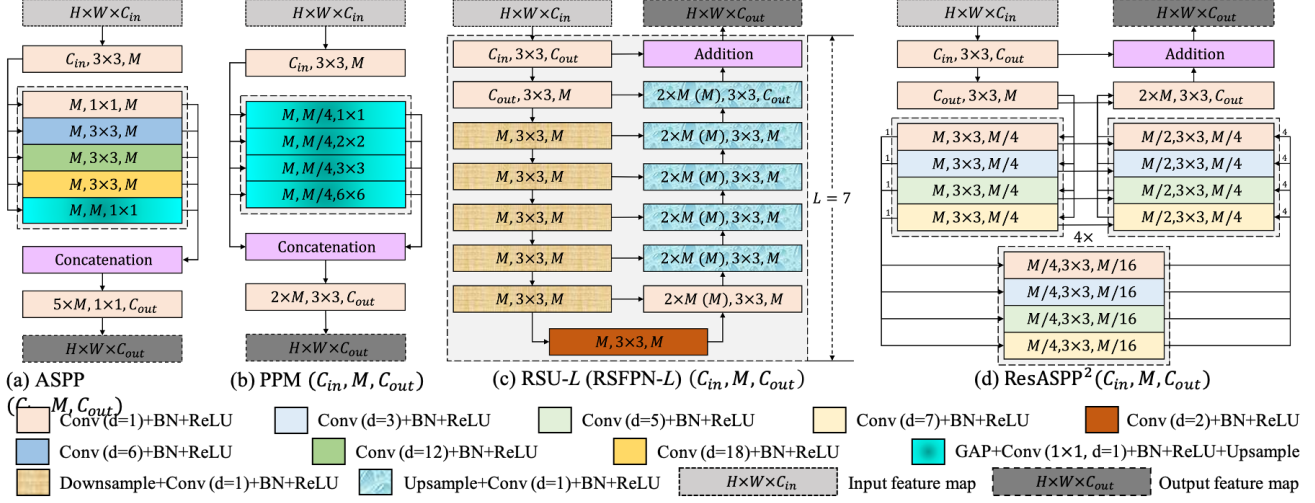


Figure 4. Illustration of existing multi-scale feature fusion module and our proposed two-level Residual nested-ASPP module: (a) ASPP-like module, (b) PPM-like module, (c) RSU module and its extension RSFPN module, where L is the number of layers in the encoder, (d) Our two-level Residual nested-ASPP module ResASPP^2 .

Residual nested-ASPP modules. Next we describe the Parallel Acceleration for DC-Net in detail. The training loss is described at the end of this section.

3.1. Divide-and-Conquer Network

The original use of the divide-and-conquer concept was to govern a nation, religion or country by first dividing it and then controlling and ruling it. Later, the same concept was applied to algorithms. The idea behind it is quite simple: divide a large or complex problem into smaller, simpler problems. Once the solutions to these smaller problems are obtained, they can be combined to solve the original problem. The Strassen algorithm [46] is an example of this concept being used. It introduces the divide-and-conquer strategy into matrix multiplication by breaking a matrix into four equally sized blocks, performing calculations recursively until the blocks can no longer be divided, and then combining the obtained solutions to obtain the solution to the original problem. Merge sort algorithm [10] works by dividing an array into two smaller arrays and sorting them recursively, and once the two smaller arrays are sorted, the algorithm merges them back together in a sorted order. These algorithms are proposed to speed up its corresponding operation process, which utilizes the advantages of parallel computing by using divide-and-conquer.

In this work, we propose a novel end-to-end network, named Divide-and-Conquer Network (DC-Net), by incorporating the concept of divide-and-conquer into the training process of salient object detection (SOD) networks. DC-Net divides the task of predicting saliency maps into n sub-tasks, each responsible for predicting different semantic information of saliency maps. To achieve this, we supervise each stage of the encoder of every subtask with distinct aux-

iliary maps, while using the same encoder for each subtask. To reduce the GPU memory cost, we add an input convolutional layer with a kernel size of 3×3 and a stride of 2 before the first stage of every subtask.

Here, we set n to 2 to build our DC-Net as shown in Fig. 3. DC-Net has 2 encoders **Encoder1** and **Encoder2**, each consisting of 4 stages (**En1.1**, **En2.1**, **En3.1**, **En4.1** and **En1.2**, **En2.2**, **En3.2**, **En4.2**), and a decoder consisting of 5 stages (**De1**, **De2**, **De3**, **De4**, **De5**). The input to each decoder stage (**De(N)**) is the concatenation of the output of **En(N).1**, **En(N).2**, and **De(N+1)**, where N is in $\{1, 2, 3, 4\}$, and the input to **De5** is the concatenation of the output of **En4.1** and **En4.2** after downsampling. Our method generates all side output predicted maps **Sup1.1**, **Sup2.1**, **Sup3.1**, **Sup4.1**, **Sup1.2**, **Sup2.2**, **Sup3.2**, **Sup4.2**, **Sup1**, **Sup2**, **Sup3**, **Sup4**, and **Sup5** from all encoder and decoder stages similar to HED [58] by passing their outputs through a 3×3 convolutional layer and a sigmoid function, and then upsampling the logits of these maps to the input image size. We choose edge maps with width 4 (only for the pixels salient in the saliency maps) and location maps, as shown in Fig. 2 (i) and (c), as target maps for two subtasks, which learn edge and location representations of salient objects respectively. The saliency map is used to supervise each decoder stage. We choose the output predicted map **Sup1** as our final saliency map.

3.2. Two-Level Residual Nested-ASPP Modules

For tasks such as salient object detection or other pixel-level tasks, both local and global semantic information are crucial. Local semantic information can be learned by shallow layers of the network, while global information depends on the size of the receptive field of the network. The most

typical methods of enlarging the receptive field are as follows. The first one is to use the atrous convolution proposed by Deeplab [3]. The atrous convolution can obtain a larger receptive field than ordinary convolution without sacrificing image resolution. The atrous spatial pyramid pooling (ASPP) (as shown in Fig. 4 (a)) consisting of atrous convolutions with different dilation rates obtains output feature maps with rich semantic information by fusing multi-scale features. The second is to use global average pooling (GAP) of different sizes similar to the pyramid pooling modules (PPM) (as shown in Fig. 4 (b)) proposed by PSPNet [66] to obtain prior information of different scales and different sub-regions, and then concatenate them with the original feature map, and after another convolutional layer, the output feature map with global semantic information is obtained. The third is to continuously obtain feature maps of different scales through downsampling, then upsample and aggregate low-level and high-level with different scales step by step like U-Net [42] and FPN [25] (as shown in Fig. 4 (c)). Their shortcomings are also obvious. ASPP has the disadvantage of sparse pixel sampling. PPM requires the original feature map to have a good feature representation. U-Net and FPN sacrifice the high resolution of the feature map in the process of downsampling and require more convolutional layers to obtain a larger receptive field, which leads to a large model size.

Inspired by the methods mentioned above, we propose a novel two-level Residual nested-ASPP module, **ResASPP²**, to capture compact multi-scale features. In theory, ResASPP² can be extended to ResASPPⁿ, where the exponent n can be set as an arbitrary positive integer. We set n to 2 as it balances performance and efficiency mostly. The structure of ResASPP²(C_{in}, M, C_{out}) is shown in Fig. 4 (d), where C_{in} , C_{out} denote input and output channels and M denotes the number of channels in the internal layers of ResASPP². Our ResASPP² mainly consists of three components:

- 1) an input convolution layer, which transforms the input feature map x ($H \times W \times C_{in}$) to an intermediate map $\mathcal{F}(x)$ with channel of C_{out} which contains local feature.
- 2) Different from the dilation rate setting $\{1, 6, 12, 18\}$ in ASPP, we set the dilation rate of each layer of ResASPP² to $\{1, 3, 5, 7\}$ to obtain more compact pixel sampling. After two-level nested-ASPP, a feature map $ASPP^2(\mathcal{F}(x))$ with channel of C_{out} is obtained, which has a larger receptive field and more multi-scale contextual information than ASPP, under a smaller dilation rate. $ASPP^2$ represents the part of Fig. 4 (d) other than the input convolutional layer.

Fig. 5 presents a comparison of the effective receptive field (ERF) [31] of various modules, including a single ASPP-like module, PPM-like module, RSU

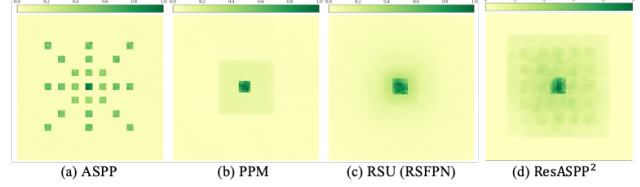


Figure 5. Comparison of the effective receptive field (ERF) of ASPP-like module, PPM-like module, RSU (RSFPN) module and our ResASPP² module.

(RSFPN) module, and our proposed ResASPP² module. ResASPP² module outperforms other modules with the largest ERF and more compact ERF than ASPP. While RSU (RSFPN) module achieves its largest receptive field on the feature map with the lowest resolution after continuous downsampling, the decay of the gradient signal is exponential, resulting in a smaller ERF of its feature map obtained from the last layer after continuous upsampling and convolution. According to [9], the ERF is proportional to $\mathcal{O}(K\sqrt{L})$, where K is the kernel size and L is the depth (i.e., number of layers). Due to the fewer layers of ResASPP², the decay of the receptive field is negligible. Although RSU (RSFPN) has a larger largest receptive field than ResASPP², the ERF of its feature map obtained from the last layer is smaller than that of ResASPP². Furthermore, ResASPP² maintains high resolution of the feature maps all the time, while RSU (RSFPN) loses detail information in the process of continuous downsampling.

- 3) a residual connection is used to fuse local features with multi-scale features through addition: $\mathcal{F}(x) + ASPP^2(\mathcal{F}(x))$.

3.3. Parallel Acceleration

One advantage of the Divide-and-Conquer approach is its potential for parallel computing, which can improve the efficiency of the network. As shown in Fig. 6, the two identical encoders responsible for different subtasks can perform forward propagation simultaneously. To fully exploit this potential, we merge these two encoders into a single encoder with the same structure (**Parallel Encoder**) by reparameterizing operations such as convolutional layers, linear layers, matrix dot products, and layer normalization. Additionally, our ResASPP² module is accelerated by a proposed operation called **Merged Convolution**, which merges parallel convolutions with the same kernel size and output size. This allows for the computation of multiple parallel convolutions in a single step, reducing the total number of operations and accelerating the processing speed.

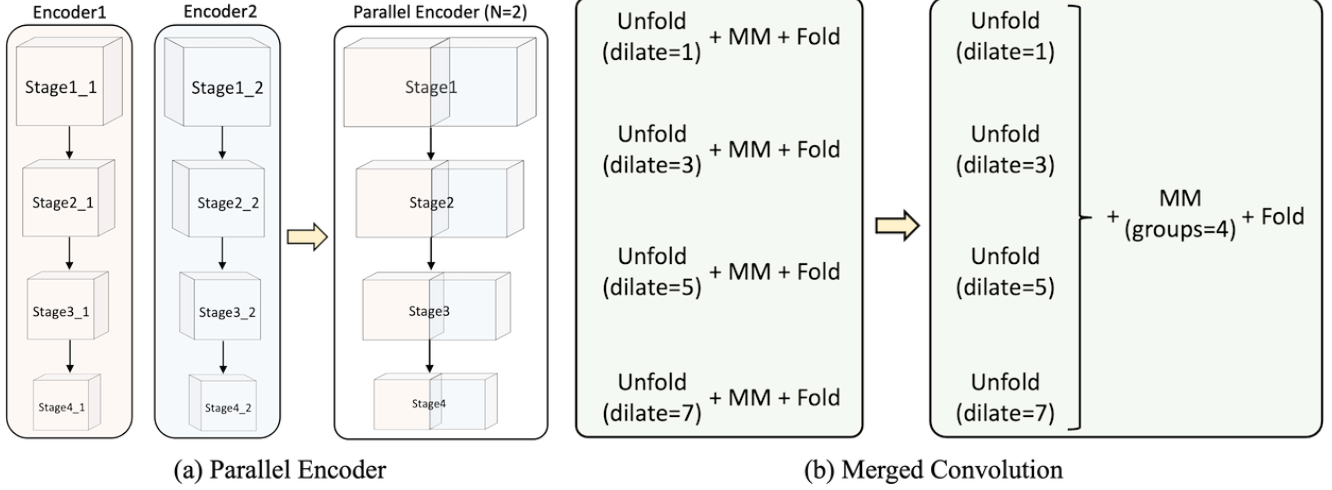


Figure 6. Illustration of the parallel encoder and merged convolution. ‘MM’ means Matrix Multiplication. A convolution operation can be separated as three parts: an unfold operation, a matrix multiplication, and a fold operation.

3.4. Loss Function

Our training loss function is defined as follows:

$$L = \sum_{e=1}^E (w_1^{(e)} l_1^{(e)} + w_2^{(e)} l_2^{(e)}) + \sum_{d=1}^D w^{(d)} l^{(d)} \quad (1)$$

In this equation, $l_1^{(e)}$ and $l_2^{(e)}$ are the losses of the side output auxiliary maps of **En(e)_1** and **En(e)_2** (referred to as **Sup(e)_1** and **Sup(e)_2** in Fig. 3), where e denotes the e_{th} encoder out of a total of E stages. $l^{(d)}$ is the loss of the side output saliency maps of **De(d)**, where d denotes the d_{th} decoder out of a total of D stages. The weights of each loss term are denoted by $w_1^{(e)}$, $w_2^{(e)}$, and $w^{(d)}$, respectively.

For each term l_1 and l_2 , we use the standard binary cross entropy to calculate the loss:

$$l_{bce} = - \sum_{(x,y)}^{(H,W)} [g(x,y) \log(p(x,y)) + (1 - g(x,y)) \log(1 - p(x,y))] \quad (2)$$

where (x,y) is the pixel coordinates and (H,W) is the height and width of the image. $g(x,y)$ and $p(x,y)$ denote the pixel values of the ground truth and predicted probability map respectively. For each term l , to take the global structure of the image into account, in addition to using the standard binary cross entropy, we also use IoU to calculate the loss:

$$l_{iou} = 1 - \frac{\sum_{(x,y)}^{(H,W)} [g(x,y)p(x,y)]}{\sum_{(x,y)}^{(H,W)} [g(x,y) + p(x,y) - g(x,y)p(x,y)]} \quad (3)$$

where the notations are the same as Eq. 2. The goal of our training process is to minimize the overall loss L .

4. Experiments

4.1. Implementation Details

In the training process, we use data augmentation including horizontal flip, random crop, and multi-scale input images. Two pretrained ResNet-34 [15] and Swin-B [29] are used as the encoders of our DC-Net-R and DC-Net-S respectively, and other parameters are randomly initialized. The loss weights w_1^e , w_2^e and w^d are all set to 1. Stochastic gradient descent (SGD) optimizer with momentum [43] is used to train our network and its learning rate is set to 0.01 for LR datasets (ResNet-34), 0.001 for HR datasets (ResNet-34), and 0.001 for LR datasets (Swin-B), other hyperparameters including momentum and weight decay are set to 0.9 and 0.0001. We set the batch size to 32 for LR datasets (ResNet-34), 4 for HR datasets (ResNet-34), and 8 for LR datasets (Swin-B) and train the network for around 60k iterations until the loss converges. In addition, we use apex¹ and fp16 to accelerate the training process. During inference, each image is first resized to 352×352 for LR datasets (ResNet-34), 1024×1024 for HR datasets (ResNet-34), and 384×384 for LR datasets (Swin-B). Our network is implemented based on PyTorch [37]. Both training and testing and other experiments are conducted on a single RTX 6000 GPU (24GB memory).

4.2. Parallel Acceleration Details

We directly implement the Merged Convolution with PyTorch without modifying the underlying code written in C language. Using the Merged Convolution and Parallel Encoder for training can result in large memory costs and low efficiency, therefore, we use Training-DC-Net and

¹<https://github.com/NVIDIA/apex>

Inference-DC-Net in training and inference phase respectively. The Training-DC-Net does not merge any operation, and the Inference-DC-Net uses Merged Convolution and Parallel Encoder. The parameters are copied from Training-DC-Net to Inference-DC-Net based on specific rules before inference.

4.3. Evaluation Metrics

To provide relatively comprehensive and unbiased evaluation of the quality of those output probability maps against the ground truth, nine different metrics including (1) Precision-Recall (PR) curves, (2) F-measure curves, (3) maximal F-measure ($\max F_\beta \uparrow$) [1], (4) Mean Absolute Error ($MAE \downarrow$), (5) weighted F-measure ($F_\beta^w \uparrow$) [33], (6) structural measure ($S_\alpha \uparrow$) [11], (7) mean enhanced alignment measure ($E_\phi^m \uparrow$) [12], (8) relax human correction efforts (HCE_γ) [39], (9) mean boundary accuracy (mBA) [7] are used:

- (1) **PR Curve** is generated using a collection of precision-recall pairs. When given a saliency probability map, its precision and recall scores are evaluated by comparing its thresholded binary mask with the actual ground truth mask. The precision and recall scores for the entire dataset are obtained by averaging the scores of individual saliency maps. By varying the thresholds between 0 and 255, a group of average precision-recall pairs for the dataset can be obtained.
- (2) **F-measure Curve** draws the change of F-measure under different thresholds. For different thresholds between 0 and 255, the F-measure value of each dataset is obtained by averaging the F-measure value computed by comparing thresholded binary mask of each saliency probability map and its corresponding ground truth mask.
- (3) **F-measure** (F_β) is a weighted harmonic mean of precision and recall:

$$F_\beta = \frac{(1 + \beta^2) \times Precision \times Recall}{\beta^2 \times Precision + Recall} \quad (4)$$

We set the β^2 to 0.3 similar to previous works [1, 40]. F_β has different values for different thresholds between 0 and 255, and we report the maximum F_β ($\max F_\beta$) for each dataset.

- (4) **MAE** is the Mean Absolute Error which is calculated by averaging pixel-wise difference between the predicted saliency map (P) and the ground truth mask (G):

$$MAE = \frac{1}{H \times W} \sum_{x=1}^H \sum_{y=1}^W |P(x, y) - G(x, y)| \quad (5)$$

- (5) **weighted F-measure** (F_β^w) is proposed to overcome the possible unfair comparison caused by interpolation flaw, dependency flaw and equal-importance flaw [27]:

$$F_\beta^w = \frac{(1 + \beta^2) \times Precision^w \times Recall^w}{\beta^2 \times Precision^w + Recall^w} \quad (6)$$

We set β^2 to 1.0 as suggested in [2], and the weights (w) is different to each pixel according to its specific location and neighborhood information.

- (6) **S-measure** (S_α) is used to evaluate the object-aware (S_o) and region-aware (S_r) structural similarity, which is computed as:

$$S_\alpha = (1 - m)S_r + mS_o \quad (7)$$

We set α to 0.5 as suggested in [11].

- (7) **E-measure** (E_ϕ^m) considers the local pixel values with the image-level mean value in one term, which can be defined as:

$$E_\phi = \frac{1}{H \times W} \sum_{x=1}^H \sum_{y=1}^W \phi(x, y) \quad (8)$$

, where $\phi = f(\xi)$ is defined as the enhanced alignment matrix, ξ is defined as an alignment matrix, and $f(x) = \frac{1}{4}(1 + x)^2$ is a simple and effective function. We report mean E-measure (E_ϕ^m) for each dataset.

- (8) **relax HCE** (HCE_γ) aims to estimate the amount of human efforts needed to correct erroneous predictions and meet specific accuracy standards in practical scenarios, which can be defined as:

$$HCE_\gamma = \text{compute_HCE}(FN', FP', TP, \text{epsilon}) \quad (9)$$

We set γ to 5 and epsilon to 2.0 as suggested in [39].

- (9) **mBA** is used to evaluate the boundary quality, and [19] shows that mBA itself cannot measure the performance of saliency detection, rather it only measures the quality of boundary itself.

4.4. Ablation Study

Ablation on Auxiliary Maps: In the auxiliary maps ablation, the goal is to find the most effective auxiliary map combination of subtasks. As shown in Table 1, we take the case of no subtask as the baseline, and we find that the performance of DC-Net-R is worse when the auxiliary maps all are saliency maps. We believe that predicting the saliency map is a difficult task, and the subtask should be simple, which may be the reason for the poor performance. Using the body and detail maps proposed in [54] as auxiliary maps

yields a performance comparable to the baseline. Multi-value maps are more challenging than binary maps, making them unsuitable as subtasks. If we assume that predicting the saliency map involves a two-step process, where the first step is predicting the background pixel value as 0 and the second step is predicting the foreground pixel value as 1, then predicting the location map containing the location information of salient objects completes the first step, which is a simple binary prediction subtask. The edge map is a commonly used auxiliary map, and we have observe that the width of the edge pixel can impact the performance of the network. Our hypothesis is that a moderate width of the edge pixel can help the network focus more on the edges and avoid introducing excessive non-edge information.

Table 1. Results of ablation study on auxiliary maps. The table compares the results when encoder1 and encoder2 are supervised by different auxiliary maps including saliency, body, detail, edge1, edge2, edge3, edge4, edge5 and location maps as shown in Fig. 2. **Cyan** means the auxiliary maps that our DC-Net adopts.

Auxiliary Map		DUTS-TE					HKU-IS				
Encoder1	Encoder2	$maxF_\beta$	MAE	F_β^w	S_α	E_ϕ^m	$maxF_\beta$	MAE	F_β^w	S_α	E_ϕ^m
-	-	.891	.040	.838	.888	.917	.940	.028	.902	.921	.950
Saliency	Saliency	.887	.040	.829	.885	.915	.939	.029	.901	.921	.950
Body	Detail	.891	.038	.837	.888	.917	.940	.029	.902	.920	.949
Edge1	Location	.894	.037	.845	.891	.921	.941	.028	.905	.921	.951
Edge2	Location	.896	.036	.845	.893	.923	.941	.028	.905	.922	.952
Edge3	Location	.897	.036	.847	.893	.923	.942	.028	.905	.921	.951
Edge4	Location	.899	.035	.852	.896	.927	.942	.027	.909	.924	.954
Edge5	Location	.895	.036	.845	.892	.922	.941	.028	.905	.922	.951

Ablation on Modules: In the module ablation, the goal is to validate the effectiveness of our newly designed two-level Residual nested-ASPP module (ResASPP²). Specifically, we fix the encoder part and the combination of subtasks (Edge4+Location) and replace each stage of the decoder with other modules in Fig. 4, including ASPP-like modules, PPM-like modules, RSU modules, and RSFPN modules. The module parameters C_{in} , M , and C_{out} of each stage of different modules are the same.

Table 2 shows the model size, FPS, and performance on DUTS-TE, HKU-IS datasets of DC-Net using different modules. Compared with RSU and RSFPN, our ResASPP² has a smaller model size when the FPS is competitive with them, and achieves better results on the datasets. Compared with the traditional two multi-scale contextual modules ASPP-like module and PPM-like module, ResASPP² greatly improves the performance on the datasets. Therefore, we believe that our newly designed ResASPP² can achieve better results than other modules in this salient object detection task.

Ablation on Parallel Acceleration: As shown in Table 3, the ablation study on parallel acceleration compares the time costs of DC-Net-R with and without acceleration of encoder or ResASPP². Training-DC-Net and Inference-DC-Net have the lowest time costs in the training phase and inference phase, respectively. As we can see, the acceler-

Table 2. Results of ablation study on modules. The structure of ASPP-like module, PPM-like module, RSU module, RSFPN module and ResASPP² module are shown in Fig. 4. **Cyan** means the module that our DC-Net adopts to the decoder.

Module	Size (MB)	FPS	DUTS-TE					HKU-IS				
			$maxF_\beta$	MAE	F_β^w	S_α	E_ϕ^m	$maxF_\beta$	MAE	F_β^w	S_α	E_ϕ^m
ASPP [3]	269.3	66	.892	.040	.826	.878	.905	.938	.032	.893	.913	.939
PPM [66]	266.5	77	.885	.039	.830	.886	.915	.939	.028	.905	.922	.952
RSU [40]	425.3	61	.894	.038	.842	.892	.920	.941	.028	.906	.923	.952
RSFPN	374.1	63	.895	.038	.844	.894	.923	.942	.027	.906	.924	.952
ResASPP²	356.3	60	.899	.035	.852	.896	.927	.942	.027	.909	.924	.954

ated encoder and ResASPP² are 5 (21) ms and 9 (13) ms faster for DC-Net-R (DC-Net-S), respectively, for a total of 14 (34) ms faster.

Table 3. Results of ablation study on parallel acceleration. ✓ and ✗ denote with and without acceleration respectively. **Cyan** and **Magenta** denote Training-DC-Net and Inference-DC-Net respectively. The batch sizes of training phase here are 12 (DC-Net-R) and 4 (DC-Net-S).

Parallel Acceleration		DC-Net-R			DC-Net-S		
Encoder	ResASPP ²	Training time (ms)	Inference time (ms)	Max batch size	Training time (ms)	Inference time (ms)	Max batch size
✗	✗	430	31	47	553	69	8
✓	✗	2055	26	46	682	48	7
✗	✓	665	22	24	619	56	6
✓	✓	2314	17	24	756	35	5

4.5. Experiments on Low-Resolution Saliency Detection Datasets

4.5.1 Datasets

Training dataset: DUTS dataset [49] is the largest and most frequently used training dataset for salient object detection currently. DUTS can be separated as a training dataset **DUTS-TR** and **DUTS-TE**, and we train our network on **DUTS-TR**, which contains 10553 images in total.

Evaluation datasets: We evaluate our network on five frequently used benchmark datasets including: **DUTS-TE** [49] with 5019 images, **DUT-OMRON** [61] with 5168 images, **HKU-IS** [20] with 4447 images, **ECSSD** [59] with 1000 images, **PASCAL-S** [22] with 850 images. In addition, we also measure the model performance on the challenging **SOC** (Salient Object in Clutter) test dataset [13] to show the generalization performance of our network in different scenarios.

4.5.2 Comparison with State-of-the-arts

4.5.2.1 Dataset-Based Analysis

We compare our DC-Net-R with 18 recent four years state-of-the-art convolution-based methods including one **RSU** based model: **U²-Net**; one **ResNet-34** based model: **BAS-Net**; two **VGG-16** [45] based model: **AFNet**, **RASNet**; six **ResNet-50** based model: **SCRN**, **BANet**, **F³Net**, **GC-PANet**, **LDF**, **RCSB**; for the other eight methods **PoolNet**, **EGNet**, **CPD**, **MINet**, **CAGNet**, **GateNet**, **ITSD**, **ICON**,

Table 4. Comparison of our method and 21 SOTA methods on DUTS-TE, DUT-OMRON, HKU-IS, ECSSD, and PASCAL-S in terms of $\max F_\beta$ (\uparrow), MAE (\downarrow), F_β^w (\uparrow), S_α (\uparrow) and E_ϕ^m (\uparrow). **Red**, **Green** and **Blue** indicate the best, second best, and third best performance. The superscript of each score is the corresponding ranking. ‘-’ means missing data.

Method	Backbone	Size (MB)	Input Size	FPS	DUTS-TE(5019)					DUT-OMRON(5168)					HKU-IS(4447)					ECSSD(1000)					PASCAL-S(850)				
					$\max F_\beta$	MAE	F_β^w	S_α	E_ϕ^m	$\max F_\beta$	MAE	F_β^w	S_α	E_ϕ^m	$\max F_\beta$	MAE	F_β^w	S_α	E_ϕ^m	$\max F_\beta$	MAE	F_β^w	S_α	E_ϕ^m	$\max F_\beta$	MAE	F_β^w	S_α	E_ϕ^m
Convolution-Based Methods																													
PoolNet-R ₁₉ [26]	ResNet-50	278.5	300×400	54	889 ⁹	0.37 ²	.817 ¹⁰	.887 ⁶	.910 ⁹	805 ¹³	.054 ⁴	.725 ¹³	.831 ¹³	.848 ¹²	936 ⁵	.030 ⁴	.888 ⁹	.919 ³	.945 ⁷	949 ⁴	.035 ⁴	.904 ⁹	.926 ⁴	.945 ⁵	879 ¹	.065 ⁷	.809 ⁷	.865 ²	.896 ⁵
SCRN ₁₉ [56]	ResNet-50	101.4	352×352	38	888 ⁸	0.040 ⁰	.803 ¹⁵	.885 ⁷	.900 ¹³	811 ¹⁰	.056 ⁰	.720 ¹⁴	.837 ⁸	.848 ¹²	934 ⁷	.034 ⁸	.876 ¹³	.916 ⁰	.935 ¹²	950 ²	.037 ⁵	.900 ¹¹	.927 ³	.939 ¹⁰	877 ²	.063 ⁵	.807 ⁹	.869 ¹	.892 ⁶
AFNet ₁₉ [14]	VGG-16	133.6	224×224	-	863 ¹⁴	0.046 ¹⁰	.785 ¹⁷	.867 ¹³	.893 ¹⁷	797 ¹⁵	.057 ⁷	.717 ¹⁶	.826 ¹⁴	.846 ¹⁴	922 ¹³	.036 ⁹	.869 ¹⁵	.905 ¹⁰	.934 ¹³	935 ¹¹	.042 ⁷	.886 ¹⁴	.913 ¹¹	.935 ¹²	863 ¹²	.070 ¹⁰	.797 ¹¹	.849 ¹²	.883 ¹²
BASNet ₁₉ [41]	ResNet-34	348.5	256×256	88	859 ¹⁵	0.048 ¹¹	.803 ¹⁵	.866 ¹⁴	.896 ¹⁶	805 ¹³	.056 ⁰	.751 ¹⁷	.836 ⁹	.865 ¹⁵	928 ¹⁰	.032 ⁶	.889 ⁹	.909 ⁹	.943 ⁹	942 ⁶	.037 ⁶	.904 ⁹	.916 ¹⁰	.943 ⁹	854 ¹⁵	.076 ¹³	.793 ¹⁴	.838 ¹⁶	.879 ¹⁵
BANet ₁₉ [47]	ResNet-50	203.2	400×300	-	872 ¹¹	0.040 ⁰	.811 ¹²	.879 ¹⁰	.913 ⁷	803 ¹⁴	.059 ⁸	.736 ¹⁰	.832 ¹²	.870 ¹⁵	931 ⁹	.032 ⁶	.886 ¹¹	.913 ⁸	.946 ⁶	945 ⁵	.035 ⁴	.908 ⁸	.924 ⁵	.948 ³	864 ¹¹	.070 ¹⁰	.802 ¹⁰	.852 ¹¹	.891 ¹⁰
EGNet-R ₁₉ [67]	ResNet-50	447.1	352×352	53	889 ⁹	0.039 ⁰	.816 ¹¹	.887 ⁹	.907 ¹¹	815 ¹⁰	.053 ³	.738 ⁹	.841 ¹⁴	.847 ¹⁵	935 ⁶	.031 ⁵	.887 ¹⁰	.918 ⁴	.944 ⁸	947 ⁵	.037 ⁵	.903 ¹⁰	.925 ⁵	.943 ⁷	865 ¹⁰	.074 ¹²	.795 ¹²	.852 ¹¹	.881 ¹⁴
CPD-R ₁₉ [55]	ResNet-50	192.0	352×352	37	865 ¹³	0.043 ⁸	.795 ¹⁶	.869 ¹²	.898 ¹⁴	797 ¹⁵	.056 ⁰	.719 ¹⁵	.825 ¹⁵	.847 ¹⁵	925 ¹²	.034 ⁸	.875 ¹⁴	.905 ¹⁰	.938 ¹⁰	939 ⁹	.037 ⁵	.898 ¹²	.918 ⁸	.942 ⁸	859 ¹⁴	.071 ¹¹	.794 ¹³	.848 ¹³	.882 ¹³
U ² -Net ₂₀ [40]	RSU	176.3	320×320	41	873 ¹⁰	0.045 ⁹	.804 ¹⁴	.874 ¹¹	.897 ¹⁵	823 ³	.054 ⁴	.757 ¹⁷	.847 ¹²	.867 ¹³	935 ⁶	.031 ⁵	.889 ⁹	.916 ⁶	.943 ⁹	951 ¹	.032 ⁶	.916 ⁷	.928 ⁶	.947 ⁴	859 ¹⁴	.074 ¹²	.792 ¹⁵	.844 ¹⁴	.873 ¹⁶
RASNet ₂₀ [53]	VGG-16	98.6	352×352	83	886 ⁷	0.037 ²	.827 ⁶	.884 ⁸	.920 ⁴	815 ¹⁰	.055 ⁵	.743 ⁸	.836 ⁹	.866 ¹⁶	933 ⁸	.030 ⁴	.894 ⁶	.915 ⁷	.950 ⁴	948 ⁴	.034 ³	.913 ⁴	.925 ⁴	.950 ²	871 ⁶	.061 ³	.816 ⁴	.861 ⁵	.898 ⁴
MI-Net ₂₀ [36]	ResNet-50	650.0	320×320	42	884 ⁸	0.037 ²	.825 ⁷	.884 ⁸	.917 ⁶	810 ¹¹	.056 ⁰	.738 ⁹	.833 ¹¹	.860 ¹⁷	935 ⁶	.029 ³	.897 ⁵	.919 ³	.952 ³	947 ⁵	.033 ²	.911 ⁶	.925 ⁵	.950 ²	866 ⁹	.064 ⁵	.809 ⁷	.856 ¹⁰	.896 ⁵
CAGNet-R ₂₀ [34]	ResNet-50	199.8	480×480	-	867 ¹²	0.040 ⁰	.817 ¹⁰	.864 ¹⁵	.909 ¹⁰	791 ¹⁶	.054 ⁴	.729 ¹²	.814 ¹⁶	.855 ¹⁰	926 ¹¹	.030 ⁴	.893 ⁷	.904 ¹¹	.946 ⁶	937 ¹⁰	.037 ⁵	.903 ¹⁰	.907 ¹²	.941 ⁹	866 ¹³	.066 ⁶	.808 ⁸	.842 ¹⁵	.893 ⁶
GATNet-R ₂₀ [68]	ResNet-50	514.9	384×384	65	888 ⁶	0.040 ⁰	.809 ¹³	.885 ⁷	.906 ¹²	818 ⁹	.055 ⁵	.729 ¹²	.837 ⁸	.855 ¹⁰	933 ⁸	.037 ⁶	.880 ¹²	.915 ⁷	.937 ¹¹	945 ⁶	.040 ⁶	.894 ¹³	.920 ⁸	.936 ¹¹	869 ¹³	.067 ⁹	.797 ¹¹	.858 ¹⁶	.886 ¹¹
ITSD-R ₂₀ [69]	ResNet-50	106.2	288×288	52	883 ⁹	0.047 ¹	.824 ⁸	.885 ⁷	.913 ⁷	821 ⁴	.061 ⁹	.750 ⁶	.840 ⁵	.865 ¹⁵	934 ⁷	.031 ⁵	.894 ⁶	.917 ⁵	.947 ⁵	947 ⁵	.034 ³	.910 ⁷	.925 ⁵	.947 ⁴	870 ⁷	.066 ⁶	.812 ⁶	.859 ⁷	.894 ⁷
GCANet ₂₀ [6]	ResNet-50	268.6	288×288	61	888 ⁶	0.038 ¹	.821 ⁹	.891 ³	.911 ⁸	812 ⁹	.056 ⁰	.734 ¹¹	.839 ⁶	.853 ¹¹	938 ³	.031 ⁵	.889 ⁸	.920 ²	.944 ⁸	948 ⁴	.035 ⁴	.903 ¹⁰	.927 ³	.946 ⁶	869 ¹³	.062 ⁴	.808 ⁸	.864 ³	.895 ⁵
LDF ₂₀ [54]	ResNet-50	100.9	352×352	63	897 ²	0.034 ¹	.845 ²	.892 ²	.925 ²	820 ⁵	.052 ²	.752 ⁴	.839 ⁶	.865 ¹⁵	939 ²	.028 ²	.904 ²	.919 ³	.953 ²	950 ²	.034 ³	.915 ³	.924 ⁴	.948 ³	874 ⁵	.060 ²	.822 ²	.863 ⁴	.903 ¹
ICON-R ₂₁ [70]	ResNet-50	132.8	352×352	53	892 ³	0.037 ³	.837 ⁴	.889 ⁴	.924 ³	825 ²	.057 ⁶	.761 ²	.844 ³	.864 ¹⁵	939 ²	.029 ³	.902 ³	.920 ²	.953 ²	950 ²	.032 ¹	.918 ¹	.929 ¹	.951 ¹	876 ³	.064 ⁵	.818 ³	.861 ⁵	.899 ³
RCSB ₂₂ [18]	ResNet-50	107.4	256×256	21	889 ⁵	0.035 ²	.840 ³	.881 ⁹	.919 ⁵	809 ¹²	.049 ¹	.752 ⁴	.835 ¹⁰	.858 ⁸	938 ³	.027 ¹	.909 ¹	.919 ³	.954 ¹	944 ⁷	.034 ³	.916 ²	.922 ²	.950 ²	875 ⁴	.059 ¹	.826 ¹	.860 ⁶	.902 ²
DC-Net-R (Ours-R)	ResNet-34	356.3	352×352	60	899 ¹	0.032 ¹	.852 ¹	.896 ¹	.927 ¹	827 ¹	.053 ³	.772 ²	.849 ¹	.876 ¹	942 ¹	.027 ¹	.909 ¹	.924 ¹	.954 ¹	949 ¹	.034 ³	.913 ⁴	.924 ⁴	.945 ⁵	874 ⁵	.066 ⁶	.814 ⁵	.857 ⁹	.892 ²
Self-Attention-Based Methods																													
VST ₂₁ [28]	T2T-ViT _{t-14}	178.4	224×224	35	890 ⁴	0.037 ⁴	.828 ⁴	.896 ⁴	.919 ⁴	824 ⁴	.058 ³	.755 ³	.850 ⁴	.871 ⁴	942 ¹	.029 ⁴	.897 ⁴	.928 ¹	.952 ⁴	951 ⁴	.033 ⁴	.910 ⁴	.932 ⁴	.951 ⁴	875 ⁴	.061 ⁴	.816 ³	.872 ⁴	.902 ⁴
ICON-S ₂₁ [70]	Swin-B	383.5	384×384	29	920 ²	0.025 ²	.886 ²	.917 ²	.954 ¹	855 ²	.043 ²	.804 ²	.869 ²	.900 ¹	951 ²	.022 ²	.925 ²	.935 ²	.968 ¹	961 ²	.023 ¹	.936 ²	.941 ²	.966 ¹	896 ²	.048 ¹	.854 ¹	.885 ²	.924 ¹
SelfReformer ₂₂ [62]	PVT	366.7	224×224	21	916 ³	0.027 ³	.872 ³	.911 ³	.943 ¹	837 ³	.043 ²	.784 ³	.861 ³	.884 ³	947 ³	.024 ³	.915 ³	.931 ³	.960 ³	958 ³	.027 ²	.926 ³	.936 ³	.957 ³	894 ³	.051 ³	.848 ²	.883 ³	.919 ²
DC-Net-S (Ours-S)	Swin-B	1495.0	384×384	29	930 ¹	0.023 ¹	.895 ¹	.925 ¹	.952 ²	857 ¹	.039 ¹	.809 ¹	.875 ¹	.898 ²	956 ¹	.021 ¹	.929 ¹	.941 ¹	.966 ²	966 ²	.023 ¹	.941 ¹	.947 ¹	.965 ²	899 ¹	.049 ²	.854 ¹	.887 ¹	.917 ³

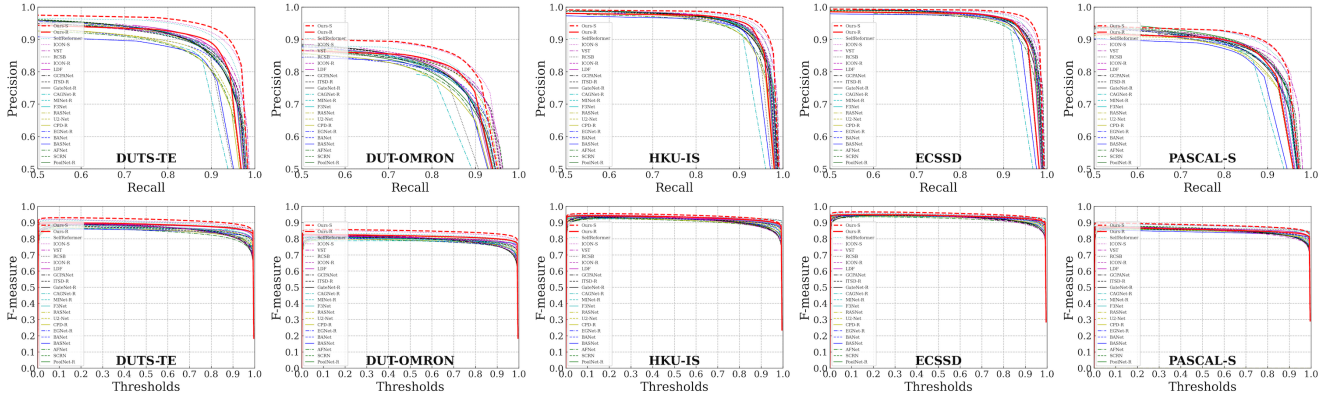


Figure 7. First row: Precision-Recall Curves comparison on five low-resolution saliency benchmark datasets. Second row: F-measure Curves comparison on five low-resolution saliency benchmark datasets.

we selected their better models based on **ResNet** or **VGG** for comparison. We also compare our DC-Net-S with 3 state-of-the-art self-attention-based methods including one **T2T-ViT_{t-14}** based model: **VST**; one **Swin-B** based model: **ICON-S**; one **PVT** based model: **SelfReformer**. For a fair comparison, we use the salient object detection results provided by the authors, and the same inference code is used to test the FPS of methods.

Quantitative Comparison: Table 4 compares five evaluation metrics including $\max F_\beta$, MAE , F_β^w , S_α and E_ϕ^m of our proposed method with others. As we can see, our DC-Net performs against the existing methods across almost all five traditional benchmark datasets in terms of nearly all evaluation metrics. Fig. 7 illustrates the precision-recall curves and F-measure curves which are consistent with Table 4. The two red lines belonging to the proposed method are higher than the other curves, which further shows the effectiveness of prior knowledge and large ERF.

Qualitative Comparison: Fig. 8 shows the sample re-

sults of our method and other eight best-performing methods and the method with the first best FPS in Table 4, which intuitively demonstrates the promising performance of our method in different scenarios.

The 1st and 2nd rows of Fig. 8 show the results for small and hidden objects. Among all methods, only our DC-Net can accurately find the location of the object in the 1st row image and segment it. The 3rd, 4th and 5th rows show the results for large objects that extend to the edges of the image and our method can accurately segment the salient objects with high confidence. The 6th, 7th and 8th rows show the scenario where there are multiple objects of the same categories that are near or far. We can find that our DC-Net is able to segment all objects accurately, while other methods miss one or more objects. The 9th, 10th and 11th rows represent the scenario of objects with thin structures. As we can observe, our DC-Net can accurately segment even better than the chair part of the ground truth of the 10th row. The 11th and 12th rows show the scenario where the image has a complex background. In this case, most of the time

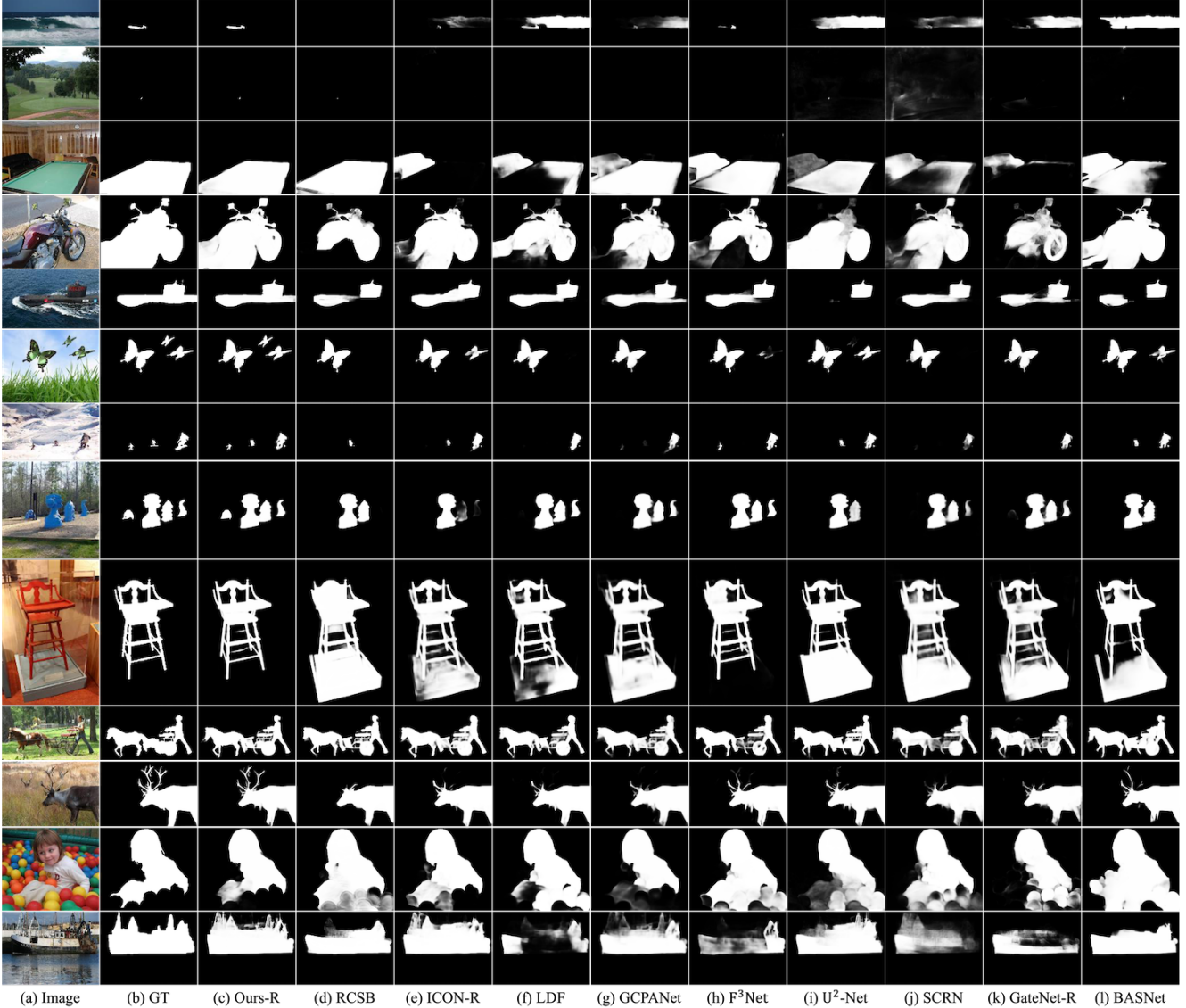


Figure 8. Low-resolution dataset-based qualitative comparison of the proposed method with nine other SOTA methods: (a) Image, (b) GT, (c) Ours-R, (d) RCSB, (e) ICON-R, (f) LDF, (g) GCPANet, (h) F³Net, (i) U²-Net, (j) SCRNet, (k) GateNet-R, (l) BASNet.

it is difficult for humans to distinguish the foreground from the background accurately. Compared with other methods, our method shows a better performance.

Failure Cases: In comparing the ground truths (GTs) and Ours-Rs of the 1_{st} row of Fig. 9, we observe that our predicted saliency maps segment some objects in addition to the salient object in the GTs. However, these objects are crucial for providing contextual information, and we believe they possess similar saliency to the salient objects in the GTs. **In the process of dataset annotation, the photographer’s intention must be considered.** For instance, the first example depicts a nail embedded in a tree trunk. In practical applications, segmenting only an overhead nail would destroy the image’s original semantic information.

The third image shows a child playing on a slide in a park, with the slide being crucial in reserving the meaning of the image, while the park is relatively unimportant and should be considered as the background. One might ask, what if I only want to keep the portrait in the image for replacing the background in practical application? We call this task as portrait matting [44] and it has corresponding datasets for the demand. For salient object detection (SOD) task, the objective is to segment the most salient object in the image, or in other words, the object that attracts your attention the most when you first look at the image. In the 2_{nd} row of Fig. 9, the salient objects in the GTs are completely opposite to the segmented objects in our predicted saliency maps. Our segmented objects are larger and have

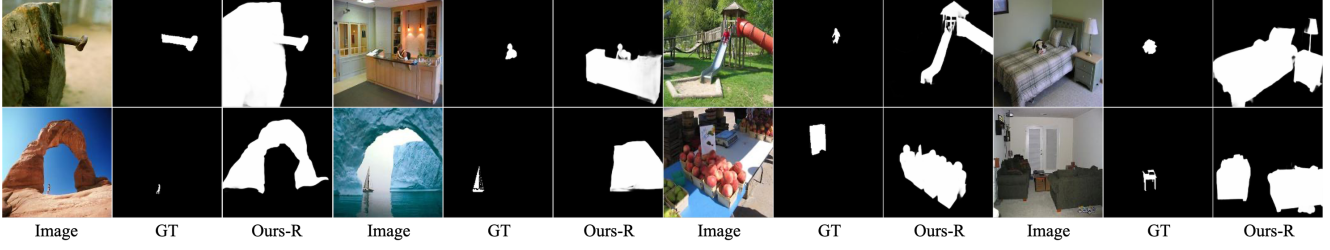


Figure 9. Failure cases of dataset-based analysis.

Table 5. Comparison of our method and 18 SOTA methods on SOC test dataset in terms of $\max F_\beta$ (\uparrow), MAE (\downarrow), F_β^w (\uparrow), S_α (\uparrow) and E_ϕ^m (\uparrow). Red, Green and Blue indicate the best, second best and third best performance. The superscript of each score is the corresponding ranking.

Attr	Metrics	Amulet	DSS	NLDF	SRM	BMPM	C2SNet	DGRL	R ³ Net	RANet	AFNet	BASNet	CPD	EGNet	PoolNet	SCRN	BANet	MINet	PiCANet	DC-Net-R
		[65]	[16]	[32]	[50]	[64]	[21]	[51]	[8]	[4]	[14]	[41]	[55]	[67]	[26]	[56]	[47]	[36]	[27]	(Ours-R)
AC	$\max F_\beta \uparrow$.752 ¹⁴	.755 ¹³	.751 ¹⁵	.804 ⁷	.791 ¹⁰	.752 ¹⁴	.785 ¹¹	.756 ¹²	.745 ¹⁶	.801 ⁸	.804 ⁷	.811 ⁵	.822 ²	.801 ⁸	.817 ⁴	.819 ³	.808 ⁶	.795 ⁹	.834 ¹
	$MAE \downarrow$.120 ¹⁶	.113 ¹⁴	.119 ¹⁵	.096 ¹¹	.098 ¹²	.109 ¹³	.081 ⁴	.135 ¹⁸	.132 ¹⁷	.084 ⁶	.083 ⁵	.089 ⁹	.085 ⁷	.093 ¹⁰	.078 ²	.086 ⁸	.079 ³	.093 ¹⁰	.076 ¹
	$F_\beta^w \uparrow$.620 ¹⁶	.629 ¹⁵	.620 ¹⁶	.690 ¹¹	.680 ¹³	.647 ¹⁴	.718 ⁸	.593 ¹⁸	.603 ¹⁷	.712 ¹⁰	.727 ⁵	.721 ⁷	.731 ³	.713 ⁹	.723 ⁶	.739 ²	.730 ⁴	.681 ¹²	.768 ¹
	$S_\alpha \uparrow$.752 ¹³	.753 ¹²	.737 ¹⁴	.791 ⁹	.780 ¹⁰	.755 ¹¹	.791 ⁹	.713 ¹⁵	.709 ¹⁶	.796 ⁶	.799 ⁵	.799 ⁵	.806 ³	.795 ⁷	.809 ²	.806 ³	.802 ⁴	.793 ⁸	.824 ¹
	$E_\phi^m \uparrow$.790 ¹⁴	.787 ¹⁵	.783 ¹⁶	.824 ¹⁰	.815 ¹¹	.806 ¹³	.853 ⁴	.752 ¹⁸	.765 ¹⁷	.852 ⁵	.842 ⁹	.852 ⁵	.854 ³	.846 ⁷	.848 ⁶	.858 ²	.843 ⁸	.814 ¹²	.867 ¹
BO	$\max F_\beta \uparrow$.814 ¹⁶	.813 ¹⁷	.835 ¹²	.853 ¹¹	.826 ¹⁵	.863 ¹⁰	.888 ⁵	.782 ¹⁸	.725 ¹⁹	.874 ⁷	.868 ⁹	.895 ⁴	.829 ¹⁴	.831 ¹³	.921 ¹	.879 ⁶	.917 ³	.919 ²	.872 ⁸
	$MAE \downarrow$.334 ¹²	.343 ¹⁵	.341 ¹⁴	.294 ¹¹	.292 ¹⁰	.257 ⁷	.207 ³	.432 ¹⁷	.440 ¹⁸	.236 ⁵	.247 ⁶	.236 ⁵	.358 ¹⁶	.339 ¹³	.217 ⁴	.261 ⁸	.175 ¹	.192 ²	.278 ⁹
	$F_\beta^w \uparrow$.625 ¹⁵	.628 ¹⁴	.635 ¹³	.679 ¹²	.683 ¹¹	.739 ⁸	.794 ³	.471 ¹⁷	.469 ¹⁸	.750 ⁶	.749 ⁷	.755 ⁵	.602 ¹⁶	.625 ¹⁵	.784 ⁴	.729 ⁹	.828 ¹	.805 ²	.699 ¹⁰
	$S_\alpha \uparrow$.589 ¹³	.577 ¹⁶	.583 ¹⁴	.628 ¹¹	.619 ¹²	.667 ⁷	.696 ⁴	.455 ¹⁸	.437 ¹⁹	.671 ⁶	.660 ⁸	.679 ⁵	.546 ¹⁷	.578 ¹⁵	.707 ³	.657 ⁹	.743 ¹	.739 ²	.637 ¹⁰
	$E_\phi^m \uparrow$.566 ¹⁴	.554 ¹⁶	.556 ¹⁵	.630 ¹²	.635 ¹¹	.674 ⁸	.736 ³	.435 ¹⁸	.423 ¹⁹	.710 ⁵	.678 ⁷	.699 ⁶	.547 ¹⁷	.572 ¹³	.716 ⁴	.663 ⁹	.769 ¹	.750 ²	.641 ¹⁰
CL	$\max F_\beta \uparrow$.781 ¹¹	.731 ¹⁶	.727 ¹⁷	.770 ¹⁴	.771 ¹³	.748 ¹⁵	.785 ⁹	.687 ¹⁸	.681 ¹⁹	.803 ⁷	.792 ⁸	.806 ⁵	.782 ¹⁰	.779 ¹²	.811 ³	.808 ⁴	.822 ²	.805 ⁶	.830 ¹
	$MAE \downarrow$.141 ¹⁰	.153 ¹²	.159 ¹³	.134 ⁸	.123 ⁷	.144 ¹¹	.119 ⁶	.182 ¹⁴	.188 ¹⁵	.119 ⁶	.114 ⁴	.112 ²	.139 ⁹	.134 ⁸	.113 ³	.117 ⁵	.108 ¹	.123 ⁷	.112 ²
	$F_\beta^w \uparrow$.663 ¹³	.617 ¹⁵	.614 ¹⁶	.665 ¹²	.678 ¹⁰	.655 ¹⁴	.714 ⁶	.546 ¹⁷	.542 ¹⁸	.696 ⁷	.724 ³	.719 ⁴	.677 ¹¹	.681 ⁹	.717 ⁵	.725 ²	.719 ⁴	.691 ⁸	.746 ¹
	$S_\alpha \uparrow$.763 ¹⁰	.721 ¹⁵	.713 ¹⁶	.758 ¹²	.76 ¹¹	.742 ¹⁴	.769 ⁸	.659 ¹⁷	.633 ¹⁸	.767 ⁹	.773 ⁷	.786 ⁴	.757 ¹³	.760 ¹¹	.795 ²	.784 ⁵	.783 ⁶	.787 ³	.798 ¹
	$E_\phi^m \uparrow$.788 ¹²	.763 ¹⁴	.764 ¹³	.792 ¹⁰	.801 ⁷	.789 ¹¹	.824 ²	.709 ¹⁶	.715 ¹⁷	.802 ⁶	.821 ⁴	.823 ³	.789 ¹¹	.800 ⁸	.819 ⁵	.824 ²	.819 ⁵	.793 ⁹	.834 ¹
HO	$\max F_\beta \uparrow$.804 ¹⁰	.789 ¹⁴	.778 ¹⁵	.800 ¹¹	.791 ¹³	.771 ¹⁶	.792 ¹²	.766 ¹⁷	.757 ¹⁸	.814 ⁹	.833 ⁴	.826 ⁷	.828 ⁶	.836 ³	.836 ³	.831 ⁵	.840 ¹	.819 ⁸	.838 ²
	$MAE \downarrow$.119 ¹⁴	.124 ¹⁶	.126 ¹⁷	.115 ¹²	.116 ¹³	.123 ¹⁵	.104 ⁹	.135 ¹⁸	.143 ¹⁹	.102 ⁸	.097 ⁵	.098 ⁶	.106 ¹⁰	.100 ⁷	.096 ⁴	.094 ³	.089 ¹	.109 ¹¹	.092 ²
	$F_\beta^w \uparrow$.688 ¹²	.660 ¹⁶	.661 ¹⁵	.696 ¹¹	.684 ¹³	.668 ¹⁴	.722 ⁸	.633 ¹⁷	.626 ¹⁸	.722 ⁸	.751 ⁴	.736 ⁷	.720 ⁹	.739 ⁶	.743 ⁵	.753 ³	.759 ²	.703 ¹⁰	.761 ¹
	$S_\alpha \uparrow$.790 ¹³	.767 ¹⁶	.755 ¹⁷	.794 ¹¹	.781 ¹⁴	.768 ¹⁵	.791 ¹²	.740 ¹⁸	.713 ¹⁹	.798 ¹⁰	.803 ⁸	.807 ⁷	.802 ⁹	.815 ⁵	.823 ¹	.819 ³	.821 ²	.809 ⁶	.818 ⁴
	$E_\phi^m \uparrow$.809 ¹³	.796 ¹⁶	.798 ¹⁵	.819 ¹⁰	.813 ¹²	.805 ¹⁴	.833 ⁸	.781 ¹⁷	.777 ¹⁸	.833 ⁸	.844 ⁵	.838 ⁷	.829 ⁹	.845 ⁴	.842 ⁶	.850 ³	.858 ¹	.817 ¹¹	.848 ²
MB	$\max F_\beta \uparrow$.680 ¹⁷	.717 ¹⁴	.698 ¹⁵	.746 ⁹	.741 ¹⁰	.692 ¹⁶	.739 ¹¹	.674 ¹⁸	.733 ¹³	.763 ⁷	.792 ²	.734 ¹²	.779 ⁵	.765 ⁶	.801 ¹	.783 ⁴	.783 ⁴	.750 ⁸	.790 ³
	$MAE \downarrow$.142 ¹⁴	.132 ¹¹	.138 ¹²	.115 ⁸	.105 ³	.128 ¹⁰	.113 ⁷	.160 ¹⁵	.139 ¹³	.111 ⁶	.106 ⁴	.104 ²	.109 ⁵	.121 ⁹	.100 ¹	.104 ²	.105 ³	.100 ¹	.109 ⁵
	$F_\beta^w \uparrow$.561 ¹⁵	.577 ¹³	.551 ¹⁶	.619 ¹¹	.651 ⁶	.593 ¹²	.655 ⁵	.489 ¹⁷	.576 ¹⁴	.626 ¹⁰	.679 ²	.655 ⁵	.649 ⁷	.642 ⁸	.690 ¹	.670 ⁴	.676 ³	.636 ⁹	.676 ³
	$S_\alpha \uparrow$.712 ¹⁴	.719 ¹³	.685 ¹⁶	.742 ¹¹	.762 ⁴	.719 ¹³	.744 ¹⁰	.657 ¹⁷	.696 ¹⁵	.734 ¹²	.754 ⁷	.753 ⁸	.762 ⁴	.751 ⁹	.792 ¹	.764 ³	.761 ⁵	.775 ²	.757 ⁶
	$E_\phi^m \uparrow$.738 ¹⁵	.753 ¹³	.739 ¹⁴	.777 ¹⁰	.812 ³	.777 ¹⁰	.823 ¹	.697 ¹⁶	.761 ¹²	.762 ¹¹	.803 ⁵	.809 ⁴	.789 ⁷	.779 ⁹	.816 ²	.803 ⁵	.793 ⁶	.812 ³	.787 ⁸
OC	$\max F_\beta \uparrow$.731 ¹³	.722 ¹⁵	.713 ¹⁶	.747 ¹¹	.747 ¹¹	.728 ¹⁴	.732 ¹²	.674 ¹⁸	.677 ¹⁷	.775 ⁵	.763 ⁹	.780 ²	.768 ⁷	.771 ⁶	.778 ³	.766 ⁸	.776 ⁴	.762 ¹⁰	.790 ¹
	$MAE \downarrow$.143 ¹³	.144 ¹⁴	.149 ¹⁵	.129 ¹¹	.119 ⁹	.130 ¹²	.116 ⁷	.168 ¹⁶	.169 ¹⁷	.109 ³	.115 ⁶	.106 ²	.121 ¹⁰	.118 ⁸	.111 ⁴	.112 ⁵	.102 ¹	.119 ⁹	.102 ¹
	$F_\beta^w \uparrow$.607 ¹⁴	.595 ¹⁵	.593 ¹⁶	.632 ¹²	.644 ¹⁰	.622 ¹³	.658 ⁵	.520 ¹⁸	.527 ¹⁷	.680 ³	.672 ⁷	.679 ⁴	.658 ⁹	.659 ⁸	.673 ⁶	.677 ⁵	.686 ²	.637 ¹¹	.708 ¹
	$S_\alpha \uparrow$.735 ¹⁴	.719 ¹⁵	.709 ¹⁶	.749 ¹¹	.752 ⁹	.738 ¹³	.747 ¹²	.653 ¹⁷	.641 ¹⁸	.771 ⁴	.750 ¹⁰	.773 ³	.754 ⁸	.756 ⁷	.775 ²	.766 ⁵	.771 ⁴	.765 ⁶	.787 ¹
	$E_\phi^m \uparrow$.762 ¹³	.760 ¹⁴	.755 ¹⁵	.780 ¹²	.799 ⁸	.784 ¹⁰	.808 ⁶	.705 ¹⁷	.718 ¹⁶	.819 ³	.810 ⁵	.818 ⁴	.798 ⁹	.800 ⁷	.800 ⁷	.808 ⁶	.821 ²	.783 ¹¹	.824 ¹
OV	$\max F_\beta \uparrow$.759 ¹⁵	.756 ¹⁶	.743 ¹⁷	.797 ¹²	.798 ¹¹	.768 ¹⁴	.808 ¹⁰	.696 ¹⁸	.689 ¹⁹	.818 ⁷	.819 ⁶	.816 ⁸	.810 ⁹	.796 ¹³	.826 ⁴	.835 ¹	.830 ²	.823 ⁵	.829 ³
	$MAE \downarrow$.173 ¹³	.180 ¹⁴	.184 ¹⁵	.150 ¹¹	.136 ⁸	.159 ¹²	.125 ³	.216 ¹⁶	.217 ¹⁷	.129 ⁶	.134 ⁷	.125 ³	.146 ⁹	.148 ¹⁰	.126 ⁴	.119 ²	.117 ¹	.127 ⁵	.126 ⁴
	$F_\beta^w \uparrow$.637 ¹³	.622 ¹⁴	.616 ¹⁵	.682 ¹¹	.701 ⁹	.671 ¹²	.733 ³	.527 ¹⁷	.529 ¹⁶	.723 ⁵	.721 ⁶	.724 ⁴	.707 ⁸	.697 ¹⁰	.723 ⁵	.751 ¹	.738 ²	.720 ⁷	.738 ²
	$S_\alpha \uparrow$.721 ¹⁵	.700 ¹⁶	.688 ¹⁷	.745 ¹³	.751 ¹⁰	.728 ¹⁴	.762 ⁷	.625 ¹⁸	.611 ¹⁹	.761 ⁸	.748 ¹¹	.765 ⁶	.752 ⁹	.747 ¹²	.774 ⁴	.779 ²	.775 ³	.781 ¹	.771 ⁵
	$E_\phi^m \uparrow$.750 ¹⁴	.737 ¹⁵	.736 ¹⁶	.778 ¹³	.806 ⁸	.789 ¹²	.828 ²	.663 ¹⁸	.664 ¹⁷	.816 ⁴	.803 ⁹	.809 ⁶	.802 ¹⁰	.795 ¹¹	.807 ⁷	.835 ¹	.822 ³	.809 ⁶	.814 ⁵
SC	$\max F_\beta \uparrow$.737 ¹²	.735 ¹⁴	.707 ¹⁷	.764 ¹⁰	.783 ⁸	.71 ¹⁶	.736 ¹³	.697 ¹⁸	.718 ¹⁵	.780 ⁹	.786 ⁷	.793 ⁴	.783 ⁸	.790 ⁵	.795 ³	.788 ⁶	.798 ²	.755 ¹¹	.816 ¹
	$MAE \downarrow$.098 ¹²	.098 ¹²	.101 ¹⁴	.090 ¹⁰	.081 ⁷	.100 ¹³	.087 ⁹	.114 ¹⁶	.110 ¹⁵	.076 ³	.080 ⁶	.076 ³	.083 ⁸						

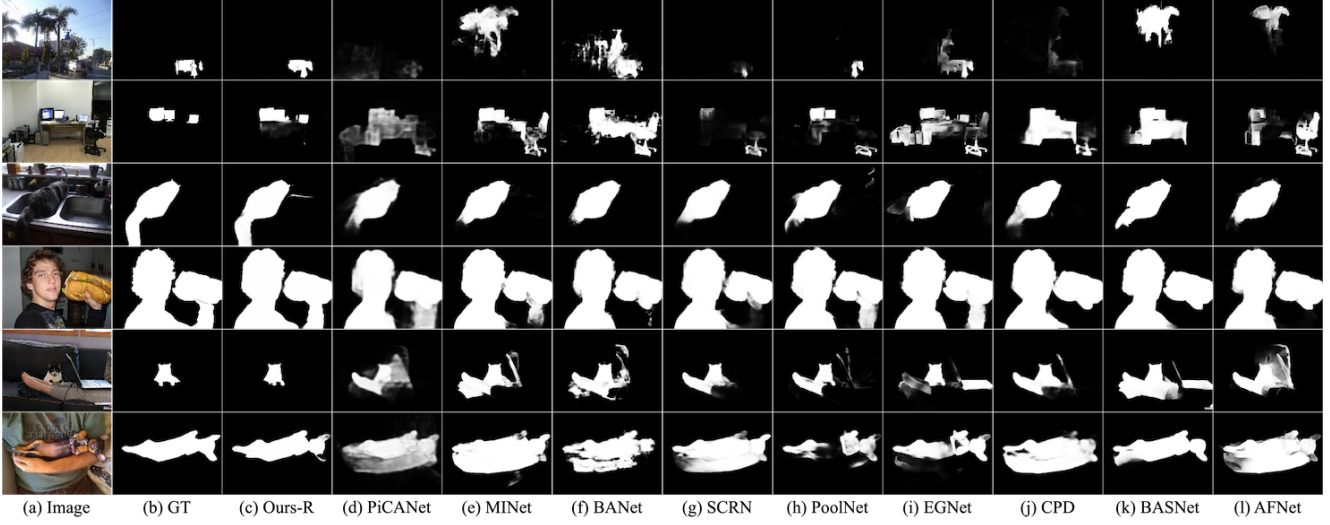


Figure 10. Low-resolution attribute-based qualitative comparison of the proposed method with nine other SOTA methods: (a) Image, (b) GT, (c) Ours-R, (d) PiCANet, (e) MINet, (f) BANet, (g) SCRNet, (h) PoolNet, (i) EGNNet, (j) CPD, (k) BASNet, (l) AFNet.



Figure 11. Failure cases of attribute-based analysis.

more distinct colors because larger and brighter objects tend to be more attention-grabbing. Moreover, we observe that in many datasets, for images that have both person and prominent landscapes, annotators tend to annotate only the person and consider the landscapes as background, even though these landscapes are what the photographer aims to highlight.

4.5.2.2 Attribute-Based Analysis

In addition to the previous 5 most frequently used saliency detection datasets, we also evaluate our DC-Net on another challenging SOC test dataset [13]. The SOC dataset divides images into the following nine groups according to nine different attributes: AC (Appearance Change), BO (Big Object), CL (Clutter), HO (Heterogeneous Object), MB (Motion Blur), OC (Occlusion), OV (Out-of-View), SC (Shape Complexity), and SO (Small Object).

We compare our DC-Net with 18 state-of-the-art methods, including Amulet [65], DSS [16], NLDF [32], SRM [50], BPM [64], C2SNet [21], DGRL [51], R³Net [8], RANet [4], AFNet [14], BASNet [41], CPD [55], EGNNet [67], PoolNet [26], SCRNet [56], BANet [47], MINet [36] and PiCANet [27] in terms of attribute-based performance.

Quantitative Comparison: Table 5 compares five evaluation metrics including $\max F_\beta$, MAE , F_β^w , S_α and E_ϕ^m of our proposed method with others. As we can see, our

DC-Net achieves the state-of-the-art performance on attributes AC, CL, OC, SC, SO and their average in terms of almost all of the five evaluation metrics, and competitive performance on HO, MB and OV. On BO attribute, DC-Net performs relatively unremarkable and the cause of it is discussed in the failure cases part below. We calculate the average of nine attributes by $Avg. = \frac{\sum_a V_a \times N_a}{\sum_a N_a}$, where A is the total number of attributes, V_a is the a_{th} metric value, and N_a is the data amount of a_{th} attribute.

Qualitative Comparison: Fig. 10 shows the sample results of our method and other nine best-performing methods in Table 5, which intuitively demonstrates the promising performance of our method in three scenarios different from those mentioned in dataset-based analysis.

The salient objects depicted in the 1st and 2nd rows of Fig. 10 possess relatively modest saliency scores when contrasted with other images, but still maintain higher saliency compared to other objects within the same image. This leads to a challenging task for models to accurately detect them. Our method is capable of accurately localizing such objects. The 3rd and 4th rows exhibit results for salient objects with low-contrast, such as the tail of the cat in the third row and the arm in the fourth row. Our DC-Net-R demonstrates robustness in accurately segmenting these objects from the background. In the 5th and 6th rows, salient objects are occluded by surrounding confusing objects. By

Table 6. Data analysis of five high-resolution datasets. Red, Green and Blue indicate the best, second best and third best.

Dataset	Number	Image Dimension				Object Complexity			
		I_{num}	$H \pm \sigma_H$	$W \pm \sigma_W$	$D \pm \sigma_D$	$IPQ \pm \sigma_{IPQ}$	$C_{num} \pm \sigma_C$	$P_{num} \pm \sigma_P$	
DIS5K [39]	5470	2513.37 \pm	1053.40	3111.44 \pm	1359.51	4041.93 \pm	1618.26	107.60 \pm	320.69
ThinObject5K [24]	5748	1185.59 \pm	909.53	1325.06 \pm	958.43	1823.03 \pm	1258.49	26.53 \pm	119.98
UHRSD [57]	5920	1476.33 \pm	272.34	1947.33 \pm	235.00	2469.12 \pm	67.11	9.62 \pm	30.71
HRSOD [63]	2010	2713.12 \pm	1041.70	3411.81 \pm	1407.56	4405.40 \pm	1631.03	5.85 \pm	12.60
DAVIS-S [38]	92	1299.13 \pm	440.77	2309.57 \pm	783.59	2649.87 \pm	899.05	7.84 \pm	5.69
								15.60 \pm	29.51
								389.58 \pm	309.29

Table 7. Comparison of our method and 8 SOTA methods on DIS-TE, ThinObject5K, UHRSD, HRSOD, and DAVIS-S in terms of HCE_γ (\downarrow), mBA (\uparrow), MAE (\downarrow), F_β^w (\uparrow), and S_α (\uparrow). Red, Green and Blue indicate the best, second best, and third best performance. The superscript of each score is the corresponding ranking.

Method	Backbone	Size (MB)	Input Size	FPS	DIS-TE(2470)					ThinObject5K(5748)					UHRSD(5920)					HRSOD(2010)					DAVIS-S(92)				
					HCE_γ	mBA	MAE	F_β^w	S_α	HCE_γ	mBA	MAE	F_β^w	S_α	HCE_γ	mBA	MAE	F_β^w	S_α	HCE_γ	mBA	MAE	F_β^w	S_α	HCE_γ	mBA	MAE	F_β^w	S_α
SCRN ₁₉ [56]	R-50	101.4	1024 \times 1024	32	1344 ⁸	.703 ⁸	.076 ⁸	.685 ⁹	.818 ⁸	250 ⁸	.744 ⁹	.099 ¹	.743 ⁷	.818 ⁷	209 ⁷	.732 ⁸	.062 ⁴	.807 ⁷	.873 ⁴	247 ⁷	.694 ⁷	.068 ²	.757 ⁷	.855 ¹	207 ⁸	.718 ³	.036 ¹	.764 ⁶	.885 ²
CPD-R ₁₉ [55]	R-50	192.0	1024 \times 1024	28	1430 ⁹	.696 ⁹	.075 ⁷	.694 ⁷	.817 ⁹	253 ⁹	.752 ⁸	.090 ⁵	.761 ⁵	.826 ⁴	218 ⁸	.728 ⁷	.062 ⁴	.814 ⁴	.872 ⁵	262 ⁸	.694 ⁷	.074 ⁴	.746 ⁵	.839 ⁴	206 ⁷	.731 ⁸	.036 ³	.765 ⁵	.880 ⁴
F ³ Net ₂₀ [53]	R-50	102.5	1024 \times 1024	58	1115 ⁵	.758 ²	.069 ³	.729 ⁴	.821 ³	188 ²	.800 ¹	.103 ⁸	.741 ⁸	.801 ⁸	173 ²	.764 ²	.067 ⁷	.804 ⁸	.855 ⁹	208 ²	.725 ²	.077 ⁵	.743 ⁶	.826 ³	160 ²	.759 ²	.040 ⁷	.738 ⁹	.852 ⁹
GCPANet ₂₀ [16]	R-50	268.6	1024 \times 1024	60	1235 ⁵	.727 ⁶	.076 ⁸	.692 ⁸	.816 ⁷	212 ⁵	.781 ⁴	.093 ⁹	.757 ⁶	.825 ⁵	192 ⁵	.748 ⁵	.066 ⁶	.799 ⁹	.863 ⁶	231 ⁵	.704 ⁶	.084 ⁷	.711 ⁸	.818 ⁷	181 ⁵	.746 ⁵	.039 ⁶	.742 ⁸	.869 ⁷
LDF ₂₁ [54]	R-50	100.9	1024 \times 1024	58	1159 ⁴	.751 ³	.070 ⁴	.730 ³	.820 ⁴	200 ³	.795 ³	.106 ⁹	.736 ⁹	.799 ⁹	180 ⁴	.761 ³	.064 ⁵	.810 ⁵	.860 ⁷	218 ⁴	.722 ⁴	.072 ³	.761 ³	.839 ⁴	173 ⁴	.755 ³	.038 ⁵	.747 ⁷	.860 ⁸
ICON-R ₂₁ [70]	R-50	132.8	1024 \times 1024	45	1337 ⁷	.711 ⁷	.072 ⁵	.715 ⁹	.809 ⁵	249 ⁷	.762 ⁷	.089 ⁴	.770 ⁴	.822 ⁶	221 ⁹	.723 ⁸	.069 ⁸	.808 ⁶	.856 ⁸	269 ⁹	.691 ⁸	.080 ⁶	.741 ⁷	.824 ⁶	206 ⁷	.737 ⁷	.035 ²	.767 ⁴	.870 ⁶
PGNet ₂₂ [57]	R-18+S-B	279.2	1024 \times 1024	31	1285 ⁶	.728 ⁵	.056 ¹	.769 ⁴	.851 ¹	226 ⁶	.779 ⁵	.072 ¹	.806 ¹	.859 ¹	196 ⁶	.758 ⁶	.041 ¹	.872 ¹	.907 ¹	238 ⁶	.723 ³	.041 ¹	.844 ¹	.898 ¹	192 ⁶	.738 ⁶	.023 ¹	.848 ¹	.917 ¹
IS-Net ₂₂ [39]	RSU	176.6	1024 \times 1024	39	1035 ²	.741 ⁴	.071 ⁵	.724 ⁴	.818 ⁶	202 ⁴	.776 ⁶	.085 ³	.778 ³	.831 ³	176 ³	.761 ³	.058 ³	.833 ³	.879 ³	211 ³	.712 ⁵	.072 ³	.757 ⁴	.839 ³	171 ³	.748 ⁴	.036 ³	.788 ³	.884 ³
DC-Net-R (Ours-R)	R-34	356.3	1024 \times 1024	55	984 ¹	.765 ¹	.063 ²	.759 ²	.840 ²	180 ¹	.796 ²	.081 ²	.786 ²	.839 ²	163 ¹	.775 ¹	.053 ²	.844 ²	.885 ²	203 ¹	.728 ¹	.068 ²	.767 ²	.846 ²	159 ¹	.763 ¹	.037 ⁴	.789 ²	.879 ⁵

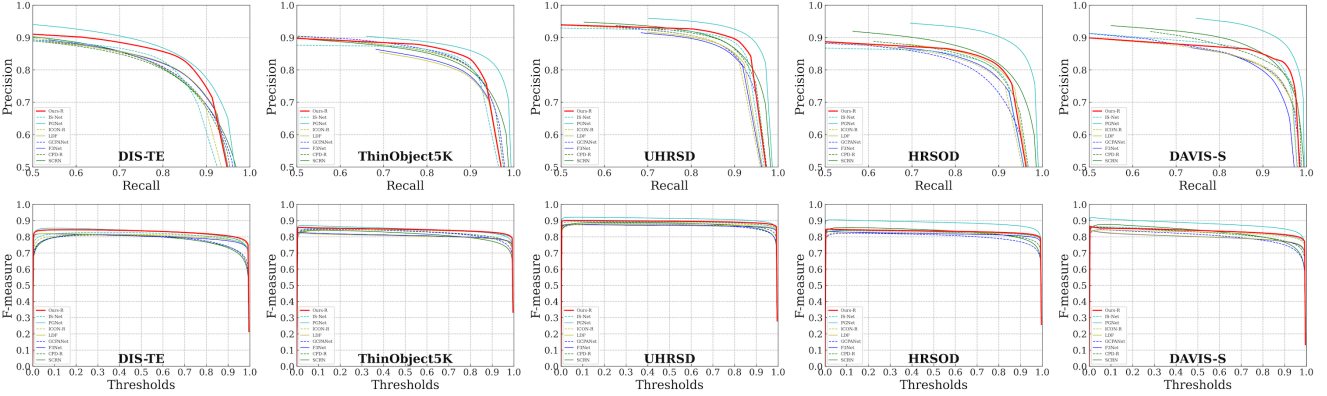


Figure 12. First row: Precision-Recall Curves comparison on five high-resolution saliency benchmark datasets. Second row: F-measure Curves comparison on five high-resolution saliency benchmark datasets.

discerning the photographer’s intent, it is apparent that the non-salient objects are not intended to draw attention in the image. Our method demonstrates accurate discrimination between salient and non-salient objects in such scenarios.

Failure Cases: In the dataset-based analysis, we show that DC-Net-R has a good ability to segment large single salient objects, while the performance of DC-Net on the BO attribute is relatively unremarkable. We find that the BO test dataset contains many images which have both large and small salient objects in different categories, such as people holding food and different kinds of food on the table shown in Fig. 11. Our findings suggest that our method is better suited for segmenting salient objects of the same category, rather than handling scenarios with multiple salient objects belonging to different categories.

4.6. Experiments on High-Resolution Saliency Detection Datasets

As the results of the methods proposed by researchers on low-resolution datasets gradually become saturated, the

development of high-resolution and high-quality (HH) segmentation has become an inevitable trend, especially for the meticulous fields of medical, aviation, and military. We suggest to use the following five datasets as training and evaluation datasets for HH methods: **DIS5K** [39], **ThinObject5K** [24], **UHRSD** [57], **HRSOD** [63] and **DAVIS-S** [38]. These datasets are all made for HH, Table 6 shows their data analysis, which is calculated following [39]. (H, W, D) and $(\sigma_H, \sigma_W, \sigma_D)$ represent the mean of the image height, width, and diagonal length and their standard deviations respectively. The object complexity of datasets is evaluated by three metrics including the *isoperimetric inequality quotient* (IPQ \uparrow) [35, 52, 60], the *number of object contours* (C_{num} \uparrow) and the *number of dominant points* (P_{num} \uparrow).

4.6.1 Datasets

Training dataset: **DIS5K** [39] can be separated as a training dataset **DIS-TR**, a validation dataset **DIS-VD** and four

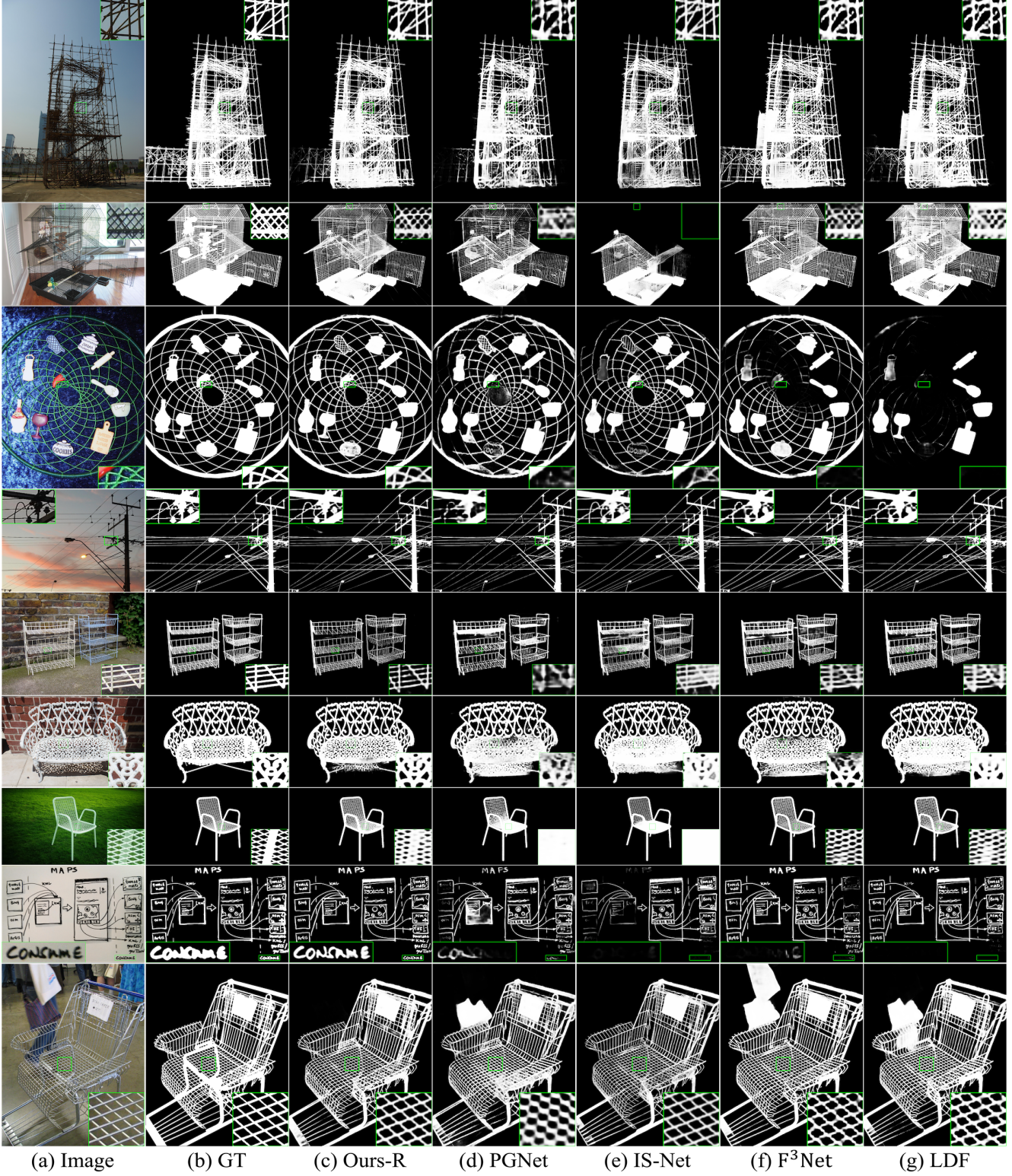


Figure 13. High-resolution qualitative comparison of the proposed method with four other SOTA methods: (a) Image, (b) GT, (c) Ours-R, (d) PGNet, (e) IS-Net, (f) F³Net, (g) LDF.

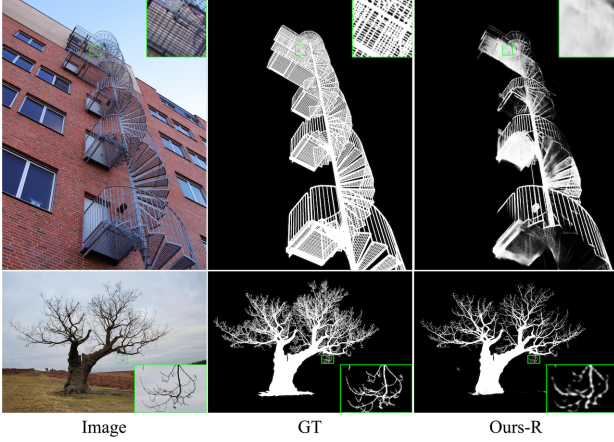


Figure 14. Failure cases of high-resolution images.

test datasets **DIS-TE1**, **DIS-TE2**, **DIS-TE3** and **DIS-TE4**. We choose **DIS-TR** as our training dataset (3000 images) because its object complexity is much higher than other datasets. We believe that when the model can accurately segment complex objects, it becomes easier to segment simple objects.

Evaluation datasets: We evaluate our network on five benchmark datasets including: **DIS-TE** with 2470 images consisting of DIS-VD, DIS-TE1, DIS-TE2, DIS-TE3 and DIS-TE4, **ThinObject5K** [24] with 5748 images, **UHRSD** [57] with 5920 images, **HRSOD** [63] with 2010 images, **DAVIS-S** [38] with 92 images.

4.6.2 Comparison with State-of-the-arts

We compare our DC-Net with 8 state-of-the-art methods including one **RSU** based model: **IS-Net**; one **ResNet-18** and **Swin-B** based model: **PGNet**; six **ResNet-50** based model: **SCRN**, **F³Net**, **GCPANet**, **LDF**, **ICON-R**, **CPD-R**, we selected their better models based on **ResNet** or **VGG** for comparison. For a fair comparison, we run the official implementation of **IS-Net** which is trained on **DIS-TR** with pre-trained model parameters provided by the author to evaluate with the same evaluation code. Moreover, we re-train **PGNet**, **SCRN**, **F³Net**, **GCPANet**, **LDF**, **ICON-R**, and **CPD-R** on **DIS-TR** based on their official implementation provided by the authors. We choose the above methods since their source codes have great reproducibility. Among them, **IS-Net** and **PGNet** are designed for high resolution, and others are designed for low resolution.

Quantitative Comparison: Table 7 compares five evaluation metrics including HCE_γ , mBA , MAE , F_β^w , and S_α of our proposed method with others, where HCE_γ and mBA are designed for evaluating the detail quality of high-resolution saliency maps. As we can see, our DC-Net-R achieves state-of-the-art performance on almost all datasets

in terms of HCE_γ and mBA , and the second-best performance on DIS-TE, ThinObject5K, UHRSD, and HRSOD in terms of MAE , F_β^w , and S_α . We find that PGNet obtain SOTA results on all datasets in terms of MAE , F_β^w , and S_α and unremarkable results on HCE_γ and mBA , which indicate that Swin Transformer outperforms ResNet in detection but may not excel in capturing details. The Fig. 12 illustrates the precision-recall curves and F-measure curves which are consistent with the Table 7.

Qualitative Comparison: Fig. 13 shows the sample results of our method and the other four best-performing methods in Table 7, which intuitively demonstrates that our method can also achieve promising results on high-resolution datasets. Ours not only accurately detects salient objects but also produces smooth and high-confidence segmentation results for fine and dichotomous parts. In contrast, the segmentation results of PGNet, F³Net, and LDF appear rough. Although the detail quality of IS-Net is competitive, the confidence level is slightly lower.

Failure Cases: As shown in Fig. 14, the spiral iron stair in 1_{st} row has densely staggered parts, resulting in a lot of holes of different sizes interspersed between the iron stairs. It is difficult for our method to segment such a dichotomous object with the input size of 1024×1024 . The branches in 2_{nd} row is a difficult case for highly accurate segmentation. It has the characteristics of irregular shape, uncertain direction, and meticulousity, which makes the confidence of predicted saliency maps low. Therefore, models that can handle higher-resolution input images to obtain detailed object structures, with acceptable memory usage, training and inference time costs on the mainstream GPUs are needed.

5. Conclusion

We propose DC-Net, a novel salient object detection method that incorporates Divide-and-Conquer into the task. DC-Net consists of an Encoder-Decoder structure, similar to U-Net, with two encoders that solve different sub-tasks: learning edge representation and location representation of salient objects. The decoder of DC-Net is composed of newly designed two-level Residual nested-ASPP (ResASPP²) modules that obtain a larger and more compact effective receptive field (ERF) compared to other multi-scale contextual modules. Additionally, we propose a parallel version of ResNet and Swin Transformer to support further research on multiple encoders. Experimental results on six public low-resolution and five high-resolution salient object detection datasets demonstrate that our DC-Net achieves competitive performance against 21 and 8 state-of-the-art methods respectively.

References

- [1] Radhakrishna Achanta, Sheila Hemami, Francisco Estrada, and Sabine Susstrunk. Frequency-tuned salient region detection. In *2009 IEEE conference on computer vision and pattern recognition*, pages 1597–1604. IEEE, 2009. 7
- [2] Ali Borji, Ming-Ming Cheng, Huaizu Jiang, and Jia Li. Salient object detection: A benchmark. *IEEE transactions on image processing*, 24(12):5706–5722, 2015. 7
- [3] Liang-Chieh Chen, George Papandreou, Iasonas Kokkinos, Kevin Murphy, and Alan L Yuille. Deeplab: Semantic image segmentation with deep convolutional nets, atrous convolution, and fully connected crfs. *IEEE transactions on pattern analysis and machine intelligence*, 40(4):834–848, 2017. 2, 5, 8
- [4] Shuhan Chen, Xiuli Tan, Ben Wang, and Xuelong Hu. Reverse attention for salient object detection. In *Proceedings of the European conference on computer vision (ECCV)*, pages 234–250, 2018. 11, 12
- [5] Shuhan Chen, Xiuli Tan, Ben Wang, Huchuan Lu, Xuelong Hu, and Yun Fu. Reverse attention-based residual network for salient object detection. *IEEE Transactions on Image Processing*, 29:3763–3776, 2020. 3, 9
- [6] Zuyao Chen, Qianqian Xu, Runmin Cong, and Qingming Huang. Global context-aware progressive aggregation network for salient object detection. In *Proceedings of the AAAI conference on artificial intelligence*, volume 34, pages 10599–10606, 2020. 3, 9, 13
- [7] Ho Kei Cheng, Jihoon Chung, Yu-Wing Tai, and Chi-Keung Tang. Cascadepsp: Toward class-agnostic and very high-resolution segmentation via global and local refinement. In *Proceedings of the IEEE/CVF Conference on Computer Vision and Pattern Recognition*, pages 8890–8899, 2020. 7
- [8] Zijun Deng, Xiaowei Hu, Lei Zhu, Xuemiao Xu, Jing Qin, Guoqiang Han, and Pheng-Ann Heng. R3net: Recurrent residual refinement network for saliency detection. In *Proceedings of the 27th International Joint Conference on Artificial Intelligence*, pages 684–690. AAAI Press Menlo Park, CA, USA, 2018. 11, 12
- [9] Xiaohan Ding, Xiangyu Zhang, Jungong Han, and Guiguang Ding. Scaling up your kernels to 31x31: Revisiting large kernel design in cnns. In *Proceedings of the IEEE/CVF Conference on Computer Vision and Pattern Recognition*, pages 11963–11975, 2022. 5
- [10] E Knuth Donald et al. The art of computer programming. *Sorting and searching*, 3:426–458, 1999. 4
- [11] Deng-Ping Fan, Ming-Ming Cheng, Yun Liu, Tao Li, and Ali Borji. Structure-measure: A new way to evaluate foreground maps. In *Proceedings of the IEEE international conference on computer vision*, pages 4548–4557, 2017. 7
- [12] Deng-Ping Fan, Cheng Gong, Yang Cao, Bo Ren, Ming-Ming Cheng, and Ali Borji. Enhanced-alignment measure for binary foreground map evaluation. *arXiv preprint arXiv:1805.10421*, 2018. 7
- [13] Deng-Ping Fan, Jing Zhang, Gang Xu, Ming-Ming Cheng, and Ling Shao. Salient objects in clutter. *IEEE Transactions on Pattern Analysis and Machine Intelligence*, 2022. 8, 12
- [14] Mengyang Feng, Huchuan Lu, and Errui Ding. Attentive feedback network for boundary-aware salient object detection. In *Proceedings of the IEEE/CVF conference on computer vision and pattern recognition*, pages 1623–1632, 2019. 1, 3, 9, 11, 12
- [15] Kaiming He, Xiangyu Zhang, Shaoqing Ren, and Jian Sun. Deep residual learning for image recognition. In *Proceedings of the IEEE conference on computer vision and pattern recognition*, pages 770–778, 2016. 6
- [16] Qibin Hou, Ming-Ming Cheng, Xiaowei Hu, Ali Borji, Zhuowen Tu, and Philip HS Torr. Deeply supervised salient object detection with short connections. In *Proceedings of the IEEE conference on computer vision and pattern recognition*, pages 3203–3212, 2017. 2, 11, 12
- [17] Bowen Jiang, Lihe Zhang, Huchuan Lu, Chuan Yang, and Ming-Hsuan Yang. Saliency detection via absorbing markov chain. In *Proceedings of the IEEE international conference on computer vision*, pages 1665–1672, 2013. 2
- [18] Yun Yi Ke and Takahiro Tsubono. Recursive contour-saliency blending network for accurate salient object detection. In *Proceedings of the IEEE/CVF Winter Conference on Applications of Computer Vision*, pages 2940–2950, 2022. 3, 9
- [19] Taehun Kim, Kunhee Kim, Joonyeong Lee, Dongmin Cha, Jiho Lee, and Daijin Kim. Revisiting image pyramid structure for high resolution salient object detection. In *Proceedings of the Asian Conference on Computer Vision*, pages 108–124, 2022. 7
- [20] Guanbin Li and Yizhou Yu. Visual saliency detection based on multiscale deep cnn features. *IEEE transactions on image processing*, 25(11):5012–5024, 2016. 8
- [21] Xin Li, Fan Yang, Hong Cheng, Wei Liu, and Dinggang Shen. Contour knowledge transfer for salient object detection. In *Proceedings of the european conference on computer vision (ECCV)*, pages 355–370, 2018. 11, 12
- [22] Yin Li, Xiaodi Hou, Christof Koch, James M Rehg, and Alan L Yuille. The secrets of salient object segmentation. In *Proceedings of the IEEE conference on computer vision and pattern recognition*, pages 280–287, 2014. 8
- [23] Zun Li, Congyan Lang, Jun Hao Liew, Yidong Li, Qibin Hou, and Jiashi Feng. Cross-layer feature pyramid network for salient object detection. *IEEE Transactions on Image Processing*, 30:4587–4598, 2021. 2
- [24] Jun Hao Liew, Scott Cohen, Brian Price, Long Mai, and Jiashi Feng. Deep interactive thin object selection. In *Proceedings of the IEEE/CVF Winter Conference on Applications of Computer Vision*, pages 305–314, 2021. 13, 15
- [25] Tsung-Yi Lin, Piotr Dollár, Ross Girshick, Kaiming He, Bharath Hariharan, and Serge Belongie. Feature pyramid networks for object detection. In *Proceedings of the IEEE conference on computer vision and pattern recognition*, pages 2117–2125, 2017. 2, 5
- [26] Jiang-Jiang Liu, Qibin Hou, Ming-Ming Cheng, Jiashi Feng, and Jianmin Jiang. A simple pooling-based design for real-time salient object detection. In *Proceedings of the IEEE/CVF conference on computer vision and pattern recognition*, pages 3917–3926, 2019. 1, 2, 3, 9, 11, 12

- [27] Nian Liu, Junwei Han, and Ming-Hsuan Yang. Picanet: Pixel-wise contextual attention learning for accurate saliency detection. *IEEE Transactions on Image Processing*, 29:6438–6451, 2020. 7, 11, 12
- [28] Nian Liu, Ni Zhang, Kaiyuan Wan, Ling Shao, and Junwei Han. Visual saliency transformer. In *Proceedings of the IEEE/CVF international conference on computer vision*, pages 4722–4732, 2021. 9
- [29] Ze Liu, Yutong Lin, Yue Cao, Han Hu, Yixuan Wei, Zheng Zhang, Stephen Lin, and Baining Guo. Swin transformer: Hierarchical vision transformer using shifted windows. In *Proceedings of the IEEE/CVF international conference on computer vision*, pages 10012–10022, 2021. 6
- [30] Shijian Lu, Cheston Tan, and Joo-Hwee Lim. Robust and efficient saliency modeling from image co-occurrence histograms. *IEEE transactions on pattern analysis and machine intelligence*, 36(1):195–201, 2013. 2
- [31] Wenjie Luo, Yujia Li, Raquel Urtasun, and Richard Zemel. Understanding the effective receptive field in deep convolutional neural networks. *Advances in neural information processing systems*, 29, 2016. 5
- [32] Zhiming Luo, Akshaya Mishra, Andrew Achkar, Justin Eichel, Shaozi Li, and Pierre-Marc Jodoin. Non-local deep features for salient object detection. In *Proceedings of the IEEE Conference on computer vision and pattern recognition*, pages 6609–6617, 2017. 11, 12
- [33] Ran Margolin, Lihi Zelnik-Manor, and Ayellet Tal. How to evaluate foreground maps? In *Proceedings of the IEEE conference on computer vision and pattern recognition*, pages 248–255, 2014. 7
- [34] Sina Mohammadi, Mehrdad Noori, Ali Bahri, Sina Ghofrani Majelan, and Mohammad Havaei. Cagnet: Content-aware guidance for salient object detection. *Pattern Recognition*, 103:107303, 2020. 2, 9
- [35] Robert Osserman. The isoperimetric inequality. *Bulletin of the American Mathematical Society*, 84(6):1182–1238, 1978. 13
- [36] Youwei Pang, Xiaoqi Zhao, Lihe Zhang, and Huchuan Lu. Multi-scale interactive network for salient object detection. In *Proceedings of the IEEE/CVF conference on computer vision and pattern recognition*, pages 9413–9422, 2020. 3, 9, 11, 12
- [37] Adam Paszke, Sam Gross, Francisco Massa, Adam Lerer, James Bradbury, Gregory Chanan, Trevor Killeen, Zeming Lin, Natalia Gimelshein, Luca Antiga, et al. Pytorch: An imperative style, high-performance deep learning library. *Advances in neural information processing systems*, 32, 2019. 6
- [38] Federico Perazzi, Jordi Pont-Tuset, Brian McWilliams, Luc Van Gool, Markus Gross, and Alexander Sorkine-Hornung. A benchmark dataset and evaluation methodology for video object segmentation. In *Proceedings of the IEEE conference on computer vision and pattern recognition*, pages 724–732, 2016. 13, 15
- [39] Xuebin Qin, Hang Dai, Xiaobin Hu, Deng-Ping Fan, Ling Shao, and Luc Van Gool. Highly accurate dichotomous image segmentation. In *European Conference on Computer Vision*, pages 38–56. Springer, 2022. 3, 7, 13
- [40] Xuebin Qin, Zichen Zhang, Chenyang Huang, Masood Dehghan, Osmar R Zaiane, and Martin Jagersand. U2-net: Going deeper with nested u-structure for salient object detection. *Pattern recognition*, 106:107404, 2020. 2, 3, 7, 8, 9
- [41] Xuebin Qin, Zichen Zhang, Chenyang Huang, Chao Gao, Masood Dehghan, and Martin Jagersand. Basnet: Boundary-aware salient object detection. In *Proceedings of the IEEE/CVF conference on computer vision and pattern recognition*, pages 7479–7489, 2019. 1, 3, 9, 11, 12
- [42] Olaf Ronneberger, Philipp Fischer, and Thomas Brox. U-net: Convolutional networks for biomedical image segmentation. In *International Conference on Medical image computing and computer-assisted intervention*, pages 234–241. Springer, 2015. 2, 5
- [43] David E Rumelhart, Geoffrey E Hinton, and Ronald J Williams. Learning representations by back-propagating errors. *nature*, 323(6088):533–536, 1986. 6
- [44] Xiaoyong Shen, Xin Tao, Hongyun Gao, Chao Zhou, and Jiaya Jia. Deep automatic portrait matting. In *Computer Vision—ECCV 2016: 14th European Conference, Amsterdam, The Netherlands, October 11–14, 2016, Proceedings, Part I 14*, pages 92–107. Springer, 2016. 10
- [45] Karen Simonyan and Andrew Zisserman. Very deep convolutional networks for large-scale image recognition. *arXiv preprint arXiv:1409.1556*, 2014. 8
- [46] Volker Strassen et al. Gaussian elimination is not optimal. *Numerische mathematik*, 13(4):354–356, 1969. 4
- [47] Jinming Su, Jia Li, Yu Zhang, Changqun Xia, and Yonghong Tian. Selectivity or invariance: Boundary-aware salient object detection. In *Proceedings of the IEEE/CVF International Conference on Computer Vision*, pages 3799–3808, 2019. 3, 9, 11, 12
- [48] Zhengzheng Tu, Yan Ma, Chenglong Li, Jin Tang, and Bin Luo. Edge-guided non-local fully convolutional network for salient object detection. *IEEE transactions on circuits and systems for video technology*, 31(2):582–593, 2020. 1
- [49] Lijun Wang, Huchuan Lu, Yifan Wang, Mengyang Feng, Dong Wang, Baocai Yin, and Xiang Ruan. Learning to detect salient objects with image-level supervision. In *Proceedings of the IEEE conference on computer vision and pattern recognition*, pages 136–145, 2017. 8
- [50] Tiantian Wang, Ali Borji, Lihe Zhang, Pingping Zhang, and Huchuan Lu. A stagewise refinement model for detecting salient objects in images. In *Proceedings of the IEEE international conference on computer vision*, pages 4019–4028, 2017. 11, 12
- [51] Tiantian Wang, Lihe Zhang, Shuo Wang, Huchuan Lu, Gang Yang, Xiang Ruan, and Ali Borji. Detect globally, refine locally: A novel approach to saliency detection. In *Proceedings of the IEEE conference on computer vision and pattern recognition*, pages 3127–3135, 2018. 11, 12
- [52] Andrew B Watson. Perimetric complexity of binary digital images: Notes on calculation and relation to visual complexity. Technical report, 2011. 13
- [53] Jun Wei, Shuhui Wang, and Qingming Huang. F³net: fusion, feedback and focus for salient object detection. In *Proceedings of the AAAI Conference on Artificial Intelligence*, volume 34, pages 12321–12328, 2020. 2, 9, 13

- [54] Jun Wei, Shuhui Wang, Zhe Wu, Chi Su, Qingming Huang, and Qi Tian. Label decoupling framework for salient object detection. In *Proceedings of the IEEE/CVF conference on computer vision and pattern recognition*, pages 13025–13034, 2020. 1, 3, 7, 9, 13
- [55] Zhe Wu, Li Su, and Qingming Huang. Cascaded partial decoder for fast and accurate salient object detection. In *Proceedings of the IEEE/CVF conference on computer vision and pattern recognition*, pages 3907–3916, 2019. 3, 9, 11, 12, 13
- [56] Zhe Wu, Li Su, and Qingming Huang. Stacked cross refinement network for edge-aware salient object detection. In *Proceedings of the IEEE/CVF international conference on computer vision*, pages 7264–7273, 2019. 1, 3, 9, 11, 12, 13
- [57] Chenxi Xie, Changqun Xia, Mingcan Ma, Zhirui Zhao, Xiaowu Chen, and Jia Li. Pyramid grafting network for one-stage high resolution saliency detection. In *Proceedings of the IEEE/CVF Conference on Computer Vision and Pattern Recognition*, pages 11717–11726, 2022. 3, 13, 15
- [58] Saining Xie and Zhuowen Tu. Holistically-nested edge detection. In *Proceedings of the IEEE international conference on computer vision*, pages 1395–1403, 2015. 4
- [59] Qiong Yan, Li Xu, Jianping Shi, and Jiaya Jia. Hierarchical saliency detection. In *Proceedings of the IEEE conference on computer vision and pattern recognition*, pages 1155–1162, 2013. 8
- [60] Chenglin Yang, Yilin Wang, Jianming Zhang, He Zhang, Zhe Lin, and Alan Yuille. Meticulous object segmentation. *arXiv preprint arXiv:2012.07181*, 2020. 13
- [61] Chuan Yang, Lihe Zhang, Huchuan Lu, Xiang Ruan, and Ming-Hsuan Yang. Saliency detection via graph-based manifold ranking. In *Proceedings of the IEEE conference on computer vision and pattern recognition*, pages 3166–3173, 2013. 1, 2, 8
- [62] Yi Ke Yun and Weisi Lin. Selfreformer: Self-refined network with transformer for salient object detection. *arXiv preprint arXiv:2205.11283*, 2022. 9
- [63] Yi Zeng, Pingping Zhang, Jianming Zhang, Zhe Lin, and Huchuan Lu. Towards high-resolution salient object detection. In *Proceedings of the IEEE/CVF International Conference on Computer Vision*, pages 7234–7243, 2019. 13, 15
- [64] Lu Zhang, Ju Dai, Huchuan Lu, You He, and Gang Wang. A bi-directional message passing model for salient object detection. In *Proceedings of the IEEE conference on computer vision and pattern recognition*, pages 1741–1750, 2018. 11, 12
- [65] Pingping Zhang, Dong Wang, Huchuan Lu, Hongyu Wang, and Xiang Ruan. Amulet: Aggregating multi-level convolutional features for salient object detection. In *Proceedings of the IEEE international conference on computer vision*, pages 202–211, 2017. 2, 11, 12
- [66] Hengshuang Zhao, Jianping Shi, Xiaojuan Qi, Xiaogang Wang, and Jiaya Jia. Pyramid scene parsing network. In *Proceedings of the IEEE conference on computer vision and pattern recognition*, pages 2881–2890, 2017. 2, 5, 8
- [67] Jia-Xing Zhao, Jiang-Jiang Liu, Deng-Ping Fan, Yang Cao, Jufeng Yang, and Ming-Ming Cheng. Egnet: Edge guidance network for salient object detection. In *Proceedings of the IEEE/CVF international conference on computer vision*, pages 8779–8788, 2019. 1, 2, 3, 9, 11, 12
- [68] Xiaoqi Zhao, Youwei Pang, Lihe Zhang, Huchuan Lu, and Lei Zhang. Suppress and balance: A simple gated network for salient object detection. In *European conference on computer vision*, pages 35–51. Springer, 2020. 2, 9
- [69] Huajun Zhou, Xiaohua Xie, Jian-Huang Lai, Zixuan Chen, and Lingxiao Yang. Interactive two-stream decoder for accurate and fast saliency detection. In *Proceedings of the IEEE/CVF conference on computer vision and pattern recognition*, pages 9141–9150, 2020. 1, 3, 9
- [70] Mingchen Zhuge, Deng-Ping Fan, Nian Liu, Dingwen Zhang, Dong Xu, and Ling Shao. Salient object detection via integrity learning. *IEEE Transactions on Pattern Analysis and Machine Intelligence*, 2022. 2, 9, 13